NTNU

Norwegian University of
Science and Technology

New catalysts for low-temperature selective catalytic reduction (SCR)

Ole Håvik Bjørkedal

Chemical Engineering and Biotechnology
Submission date: June 2016
Supervisor: Magnus Rønning, IKP

Norwegian University of Science and Technology
Department of Chemical Engineering

Abstract

Mesoporous alumina with a regular pore structure and high surface area was prepared using a sol-gel method with a structure-guiding surfactant. The typical diameter of the pores were measured to be 4-6 nm, with narrow pore size distributions. The alumina samples was found to have a typical specific surface area of 300 $m^2\,g^{-1}$

Modification of the acidic properties of the mesoporous alumina was attempted by introducing a solid acid, $H_3PW_{12}O_{40}$ (abbrv. HPW). Alumina-HPW composites with HPW content of 25% and 50% was prepared by introducing HPW directly in the sol-gel synthesis. The composites had pore size similar to mesoporous alumina. High HPW content lead to decrease in pore volume and surface area.

The pore structure, composition and surface properties of the mesoporous alumina and alumina-HPW composites was characterized by BET, XRD, XRF and S(T)EM. Acidic properties were characterised by FT-IR with pyridine adsorption.

Mesoporous alumina was found to exhibit Lewis acidic character, which seemed to decline with decreasing alumina content for the composites. No indication of Brønsted acidic activity was found in the IR-spectra, but several factors indicate that contaminants like water have affected the measurements. Therefore, no conclusion regarding the effect of HPW on the acidity of the composite was reached.

Samandrag

Mesoporøs alumina med regulær porestruktur og stort overflateareal vart framstilt ved ei sol-gel metode med ein surfaktant som strukturstyrande komponent. Porane vart målt til å vere jamstore i høg grad, med ein typisk diameter på mellom 4 og 6 nm. BET overflateareal vart målt til om lag 300 $m^2\,g^{-1}$.

$H_3PW_{12}O_{40}$ (forkorta HPW) vart innført i den mesoporøse aluminaen for å undersøke moglegheiter for å justere syreeigenskapane til materialet.HPW vart introdusert direkte i sol-gel-syntesen. Alumina-HPW kompositttar vart framstilt med 25% og 50% HPW-innhald utan større innverknad på porestorleik samanlikna med mesoporøs alumina. Høgt HPW innhald førte til noko redusert porevolum og overflateareal.

Porestruktur, samansetning og overflateeigenskapar vart karakterisert ved BET, XRD, XRF og S(T)EM. Syreeigenskapar vart karakterisert ved FT-IR med pyridin-adsorpsjon.

Mesoporøs alumina fekk påvist Lewis-syrlege eigenskapar av FT-IR undersøkingane. Desse ser ut til å avta i styrke for synkande alumina-innhald i kompositttane. Det vart ikkje funne teikn på Brønsted-syrleg aktivitet i nokon av prøvene, men fleire faktorar tydar på at ureiningar som vatn kan ha påverka desse målingane. På grunnlag av dette kunne ikkje effekten av HPW på syreeigenskapane til kompositttane slås fast.

Preface

I would like to thank my supervisor, Professor Magnus Rønning, for his patience and guidance during the work on this thesis.

Thanks to Xavier Auvray and Ata ul Rauf Salman for assisting with experimental methods and data interpretation. I am also very grateful to Kristin Høydalsvik for the indispensable help she has provided with XRD measurements. Cristian Ledesma Rodriguez and Karin Wiggen Dragsten deserve thanks for their training and assistance in various experimental apparatus, and the staff at NTNU Nanolab for their training and support.

Finally, I would like to thank family and friends for their patient support, and especially my fellow masterstudents for contributing to a great working environment this semester

The Research Council of Norway is acknowledged for the support to NTNU NanoLab through the Norwegian Micro- and Nano-Fabrication Facility, NorFab (197411/V30).

I declare that this is an independent work according to the exam regulations of the Norwegian University of Science and Technology.

Ole Håvik Bjørkedal June 10, 2016, Trondheim

Contents

Abstract **i**

Samandrag **iii**

Preface **v**

List of Figures **x**

List of Tables **xi**

List of Symbols **xiii**

Abbreviations **xv**

1 Introduction **1**
1.1 Background 2
1.2 Ordered mesoporous alumina in catalysis 3

2 Theory **5**
2.1 Sol-Gel synthesis of metal oxides 6
2.2 Characterization 9
2.2.1 X-Ray Diffraction 9
2.2.2 X-Ray Fluorescense 9
2.2.3 BET physisorption 10
2.2.4 Infrared Spectroscopy 13
2.2.5 Scanning Electron Microscopy (SEM) 15

3 Methods **19**

3.1 Preparation of Ordered Mesoporous Alumina and HPW-Alumina composites . . . 20
3.2 Characterization . . . 21
3.2.1 X-Ray Diffraction . . . 21
3.2.2 X-Ray Fluorescence (XRF) . . . 21
3.2.3 BET Physisorption . . . 21
3.2.4 IR-spectroscopy . . . 22
3.2.5 S(T)EM . . . 23

4 Results **25**
4.1 Characterization . . . 26
4.1.1 XRF . . . 26
4.1.2 BET . . . 26
4.1.3 XRD . . . 44
4.1.4 FT-IR . . . 47
4.1.5 S(T)EM . . . 55

5 Discussion **65**
5.1 BET/BJH analysis . . . 66
5.2 XRD . . . 66
5.3 FT-IR . . . 68
5.4 S(T)EM . . . 69
5.5 Pore size and structure . . . 70
5.6 Surface acidic properties . . . 71

6 Conclusion **73**

7 Further work **75**

A Calculations **81**
A.1 Preparation of Al-HPW composite . . . 81
A.2 Bragg diffraction angle calculation . . . 82

B FT-IR **83**
B.1 IR reference spectra . . . 83

C Risk Assessment **87**

List of Figures

2.1 Principle of alumina synthesis 8
2.2 Illustration of Bragg's law 10
2.3 IUPAC Type I Adsorption Isotherm 11
2.4 IUPAC Type IV Adsorption Isotherm 12
2.5 Overview of signals generated in S(T)EM 16

3.1 PFD of FT-IR setup 24

4.1 BET Isotherm γ-Al_2O_3 27
4.2 BJH γ-Al_2O_3 28
4.3 BET Isotherm m-Al_2O_3_1 29
4.4 BJH m-Al_2O_3_1 30
4.5 BET Isotherm m-Al_2O_3_2 31
4.6 BJH m-Al_2O_3_2 32
4.7 BET Isotherm m-Al_2O_3_3 33
4.8 BJH m-Al_2O_3_3 34
4.9 BET Isotherm 25HPW 35
4.10 BJH Pore Distribution 25HPW 36
4.11 BET Isotherm 50HPW1 37
4.12 BJH Pore Distribution 50HPW1 38
4.13 BET Isotherm 50HPW2 39
4.14 BJH Pore Distribution 50HPW2 40
4.15 Comparison of BET 50HPW 41
4.16 Comparison BJH Pore Distribution 50HPW 42
4.17 Comparison BJH Pore Distribution All 43
4.18 XRD mesoporous aluminas 44
4.19 XRD Diffractogram of HPW/Al composites 45

4.20 Dehydrated XRD 46
4.21 Small Angle XRD 47
4.22 IR-spectrum 1435:1640 cm^{-1} 48
4.23 Integrated peak areas 1400:1480 cm^{-1} 49
4.24 Integrated peak areas 1560:1620 cm^{-1} 50
4.25 Pyridine desorption m-Al_2O_3_1 51
4.26 Pyridine desorption 25HPW 52
4.27 Pyridine desorption 50HPW 53
4.28 Pyridine desorption HPW 54
4.29 SE image of pore structure m-Al_2O_3_1 56
4.30 Close-up of pores in m-Al_2O_3_1 57
4.31 SE image of 25HPW surface 1 58
4.32 SE image of25HPW surface 2 59
4.33 25HPW surface 60
4.34 25HPW elemental mapping 61
4.35 Pore structure 50HPW1 62
4.36 50HPW EDX Overview 63
4.37 50HPW1 Elemental mapping 64

B.1 Example Background spectrum 84
B.2 IR transmittance of water 85
B.3 IR spectra 30 min TOS full spectrum 86

List of Tables

2.1 Common IR bands of pyridine 15

3.1 Samples, HPW %, calcination time 20

4.1 XRF results of HPW-alumina 26
4.2 Key BET/BJH results 27

5.1 Assignment of peaks in IR-spectra 68

List of Symbols

Symbol	Dimension	Description
A	µA	SEM probe current
D	-	Dispersion of active metal on support.
d	Å	Lattice plane distance
K	-	Constant in Scherrer equation
$< L >$	nm	Crystal diameter
m_i	g	Mass of component i
$M_{m,i}$	$\mathrm{g\,mol^{-1}}$	Molar mass of component i
n	-	Order of reflection in Bragg's law
n_i	mol	Molar amount of component i
N_0	-	Amount of molecules
P	mmHg	Pressure
P_0	mmHg	Equilibrium pressure
r	cm	Radius
R	$\mathrm{J\,K^{-1}\,mol^{-1}}$	Universal Gas Constant
V_i	$\mathrm{cm^3}$	Volume of component i.
V_0	$\mathrm{cm^3}$	Volume adsorbed in first BET monolayer
$\bar{V}$	$\mathrm{cm^3}$	Molar Volume
V_{acc}	kV	SEM Acceleration Voltage
v_{absorbed}	$\mathrm{mL\,g^{-1}}$	Specific pore volume
$wt\%$	-	Weight percentage
x_i	-	Mass fraction of component i.
α	$\mathrm{cm^{-3}}$	Slope of BET isotherm linear plot
β	-	Width of XRD-peak
η	$\mathrm{cm^{-3}}$	Intercept of BET isotherm linear plot
ν	$\mathrm{s^{-1}}$	Electromagnetic frequency
$\bar{\nu}$	$\mathrm{cm^{-1}}$	Wavenumber
λ	Å	Wavelength
σ	$\mathrm{N\,m^{-1}}$	Surface tension
θ	-	Angle
χ	-	Ratio of desorption rate constants for second and first BET monolayer

Abbreviations

Abbreviation	Description
ATR	Attenuated Total Reflection
a.u.	Arbitrary Unit
Avg.	Average
BET	Braunauer, Emmett, Teller
BJH	Barrett, Joyner, Halenda
BSE	Backscattered Electrons
DRIFTS	Diffuse Reflectance Fourier Transform Spectra
EISA	Evaporation-Induced Self-Assembly
EDX	Energy-dispersive X-ray spectroscopy
HPW	Tungstophosphoric Acid $H_3PW_{12}O_{40}$x26 H_2O
IUAPC	International Union of Pure and Applied Chemistry
IR	Infrared
LNG	Liquefied Natural Gas
NSR	NOx Storage and Reduction
NOx	Nitrous Oxides
py	Pyridine
PFD	Process Flow Diagram
SCR	Selective Catalytic Reduction
SE	Secondary Electron
SEM	Scanning Electron Microscopy
S(T)EM	Scanning (Transmission) Electron Microscopy
SOx	Sulfuric Oxides
VOC	Volatile Organic Compounds
XRD	X-Ray Diffraction
XRF	X-Ray Fluorescence

Chapter 1

Introduction

More efficient and environmental friendly propulsion is in increasing demand in the transportation sector, in accordance with environmental and economical concerns and expectations of more stringent regulations on emissions. Marine transportation has traditionally used heavy fuel oil as its primary energy source, as it is cheap, readily available and reliable. Emissions of carbon or Nitrous Oxides (NOx) have not been subject to much regulation in international waters to date. However, regulations on carbon and NOx-emissions are expected to be stricter in the future

With the increase in production of oil and natural gas in North America, natural gas is cheaply available on the market. Liquefied Natural Gas (LNG) is being considered as a reasonable alternative to heavy fuel oil, with advantages such as cleaner and more efficient engines. With higher engine efficiency comes lower exhaust temperature. Traditional NOx-abatement catalysts are expected to be less effective at lower temperatures, creating a need for a new efficient catalytic system adapted to modern maritime propulsion systems.

The goal of this thesis is to develop an ordered mesoporous alumina (OMA) with a regular pore structure. Tungstophosphoric Acid ($H_3PW_{12}O_{40}$, abbreviated HPW) will be introduced in an attempt to tune the surface acidity of the material. The alumina and the alumina-HPW composites will be characterized with emphasis on their pore size and structure, surface properties and acidity.

1.1 Background

The marine transport sector has traditionally relied on heavy fuel oil as their primary fuel source. Heavy fuel oil has a high carbon density which leads to higher CO_2 emissions. As there has not been much regulation on emissions in maritime transport, there has not been much focus on limiting emissions with regards to CO_2, NOx, SOx and other pollutants. However, with an increasing global temperature and greenhouse effect causing climate change, stricter emission regulation and environmental policies should be expected.

The increase of shale gas production in the US, and the decrease in global oil price has driven the price of LNG downwards. LNG has a lower carbon density than fuel oil, and may prove to be a more efficient and environmentally friendly fuel for maritime propulsion.

Although LNG-propulsion emits less CO_2, SOx, Volatile Organic Compounds (VOCs) and particulars than traditional fuel oil, the combustion process will lead to NOx-formation which must be controlled. The release of uncombusted methane, also known as methane-slip, must also be avoided, as methane has 20 times as high greenhouse gas potential as CO_2.

Emissions of NOx is problematic for the environment as NOx is known to cause acid rain, ground level ozone formation, and is regarded as a human health hazard. NOx is formed spontaneously when air is heated to temperatures above 1300°C, which includes most combustion processes, regardless of fuel source.

Engines are required to perform under a range of loads and operational conditions. A central factor with regards to NOx-emissions is the air/fuel-ratio (often referred to as the λ-number) of the combustion. A stoichiometric relation between air and fuel ($\lambda_{\text{molar}} \approx 1$) is optimal with regards to low NOX-emissions, but may not always be the best choice for performance or methane slip. Under continuous operation, the air/fuel ratio will usually vary depending on what's required of the engine. Therefore, the NOx-abatement system must be able to perform under a wide range of operating conditions.

Selective Catalytic Reduction (SCR) and NOx-storage and reduction (NSR) are common methods for NOx-abatement in oxygen-rich flue gas. The principle of NSR is to store NOx in solid oxides during lean conditions, in order to release and reduce the NOx during rich conditions. NSR is mostly used in vehicles,

where the flue gas composition may vary from lean to rich composition over time. [1, p.395-396].

Selective Catalytic Reduction (SCR) is a well established technology for NOx-reduction that has been successfully applied in the industrial and automotive sector. SCR uses a reduction agent (e.g. ammonia) to reduce NOx. Modern engines are often designed to operate with an air surplus for maximum efficiency. The oxygen surplus leads to an oxidative environment in the exhaust, necessitating a reducing agent to reduce NOx.

Traditional SCR catalysts consists of a transition or noble metal dispersed on a porous support. Vanadia is one of the most common metals for SCR applications. Vanadium is toxic [2], and vanadia catalysts require a high temperature to be active [3]. Cu- and Fe-exchanged zeolites have resently been found be promising SCR catalysts [4]. Zeolites, mixed Al and Si oxides, are interesting materials for catalytic purposes, as they exhibit a regular pore structure, high surface area and surface acidity [1]. Recently, similar regular structures of porous alumina has been synthesized, seems to have properties well suited for catalytic purposes [5, 6].

1.2 Ordered mesoporous alumina in catalysis

Ordered Mesoporous Alumina (OMA) is a form of Al_2O_3 which has a narrow pore size distribution and a regular pore size. Mesopores are defined by IUPAC as pores at a size between 2 nm to 50 nm in diameter [7]. Transitional aluminas, such as γ-Alumina, typically have larger pores, closer to the macropore range (larger than 50 nm).

The synthesis of the first ordered mesoporous silica, MCM-41 by Mobile Research and Development [8], opened new possibilities for development of more efficient catalyst supports. OMA has recently been produced and studied by several researchers ([5, 6, 9–12] a.o.), and has shown good promise for catalytic purposes, especially due to their high surface area and well defined pore structure.

Evaporation-Induced Self-Assembly (EISA) is a simple method for synthesis of specific structures on a nanometer scale. Solids are produced through a sol-gel process while surfactants (in the form of micelles) are present as templates

for the pore structure [5, 6, 13]. This method has proven to be a simple and reproducible way of producing mesoporous aluminas [5, 6, 10, 14].

Alumina has been used in acid-catalysed processes, such as catalytic cracking, due to it's surface acidic properties. The acidic strength of alumina is dependent on the phase and structure. In order to enhance or tune the surface acidity of alumina, various acidic modifiers have been used.

Hetero Polyacids (HPA) is a collective term for acidic polyoxometallates. Polyoxometallates are metal oxides containing more than one metal atom [15, sec 18.8]. Hetero polyacids have been found to have acidic properties beneficial to several catalytic processes. HPA is known to be thermally, oxidatively and hydrolytically stable [6], as well as a promising storage component for NOx [16, 17]. Incorporating an HPA may allow for fine tuning of the surface acidity of the resulting alumina-HPA composite, much due to their stability and strong Brønsted acidic character [18], and thus maximize the efficiency of the catalyst for acid-catalyzed reactions. Armatas et.al. (2010) [6] found such composites to be highly efficient for acidic catalysis.

Chapter 2

Theory

Theoretical background information for experimental methods and analyses in the thesis is presented in this chapter. Section 2.1 focuses on the principles for catalyst preparation via sol-gel synthesis, while Section 2.2 contains the fundamental theoretical principles for all methods used to characterize the catalysts.

2.1 Sol-Gel synthesis of metal oxides

Sol-Gel synthesis of metal oxides or supported metal is a method for catalyst preparation based on the formation of a solid metal oxide from a *sol* of precursor materials. An advantage of this method compared to e.g. impregnation, is the option of introducing the active metal component simultaneously with the preparation of the support material. Another advantage is the possibility to control the structure of the material as it forms, using a structure directing agent. This enables synthesis of highly ordered materials of specific structure.

A *sol* is a term used for a suspension of colloidal particles in a liquid, while a gel may be defined as a continuous phase of colloidal dimensions [19, p.165]. Porous metal oxides may be formed through sol-gel synthesis where M-O-M bonds are formed from a colloidal solution in a polymerization process.

Metal alkoxides (M(OR)x, where R is an alkyl group) are common precursors as they are easily activated by acid- or base-catalysed hydrolysis (2.1) where a hydroxyl ion bonds to the metal atom [19, p.166].

$$\mathrm{M(OR)x} + \mathrm{H_2O} = \mathrm{HO{-}M(OR)_{x-1}} + \mathrm{ROH} \tag{2.1}$$

Two hydrolyzed molecules may form a bond by a condensation reaction, yielding a larger molecule and water (2.2) or an alcohol (2.3). These reactions may continue to propagate and form large chains of metal oxides, eventually forming a gel.

$$\mathrm{(OR)_{x-1}MOH} + \mathrm{HO{-}M(OR)_{x-1}} = \mathrm{(OR)_{x-1}M{-}O{-}M(OR)_{x-1}} + \mathrm{H_2O} \tag{2.2}$$

$$\mathrm{(OR)_{x-1}MOR} + \mathrm{HO{-}M(OR)_{x-1}} = \mathrm{(OR)_{x-1}M{-}O{-}M(OR)_{x-1}} + \mathrm{ROH} \tag{2.3}$$

The wet gel is dried to remove the solvent and obtain a solid structure. Solid gels are commonly classified as either xerogel or aerogel depending on the drying conditions. Xerogels are gels that are dried by ordinary evaporation of the solvent, while gels dried under supercritical conditions are called aerogels. Solvent evaporation may cause some capillary strain on the pore walls, leading to local collapses and changes in structure. Aerogels have a structure more resemblant of the wet gel structure, as supercritical drying does not cause capillary strain [20].

In order to produce an ordered structure, e.g. homogenous pore size, a structure directing surfactant may be introduced as a copolymer. When the concentration of a surfactant in a sol reaches a certain level, the critical micelle concentration (cmc), the surfactant will arrange itself into micelles [21, chap. 8.3]. Micelles are groups of surfactant molecules gathered spontaneously to minimize interfacial tension between the surfactants and the sol. The micelles arrange themselves with the polar parts of the molecule pointing outwards towards the polar sol, while the non-polar parts are pointed inwards to each other. (Illustrated in part 1-2 of Figure 2.1). The shape of the micelles is dependent on the surfactant molecule, but spherical and cylindrical shapes are common [21, chap. 8.3].

Cylindrical micelles are well suited as structure directors for production of regularly sized pores in a solid material. As the micelles form, the gel solidifies around the micelles, using them as a template. An illustration of this process is provided in Figure 2.1. Such processes are often referred to as Evaporation-Induced Self-Assembly (EISA). As the solvent evaporates, the surfactant concentration approaches cmc, which leads to spontaneous formation of micelles [13].

The dry gel is finally stabilized by calcination in air or oxygen at an appropriate temperature. Most porous materials are prone to structural changes, such as phase change or sintering, if exposed to high temperature. Such changes may involve loss of surface area, pore wall collapse or recrystallization, possibly with significant loss of activity. This step also serves to remove any remains of the template polymer or other organic molecules from the synthesis [20]. Calcination temperature should be sufficiently high to ensure the removal of all organic species, but not so high that it causes sintering or loss of structure (commonly around 400-500 °C) [19, p.181].

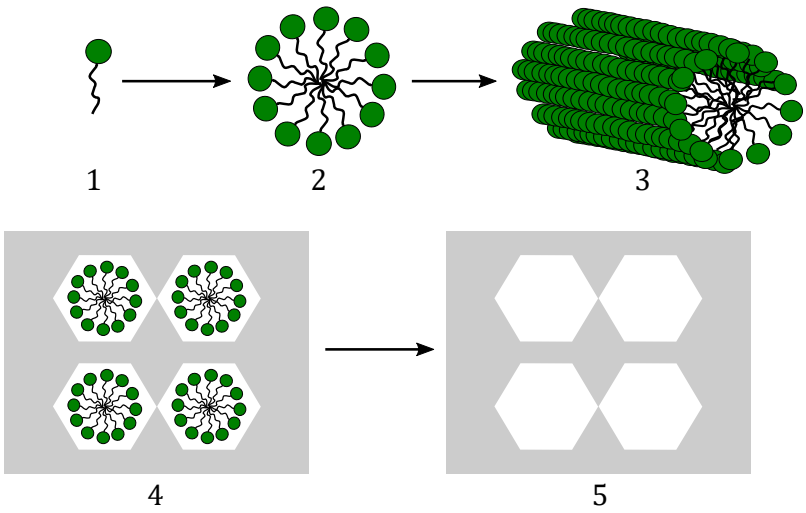

Figure 2.1: The principle behind the synthesis of regular mesoporous alumina using a surfactant as structure-directing agent. 1: Surfactants with polar heads (green) and non-polar tails (black) exists in a sol. 2: At a certain concentration, the surfactants form micelles which orients the polar head towards the polar sol, and the nonpolar parts in towards themselves to relieve van der Waal tensions. 3: Several surfactants group together in a cylindric micelle structure. 4: The alumina gel (grey) forms around the cylindric micelles. 5: The micelles are removed by calcination, and the alumina structure with it's regular pore structure is left. The illustration is inspired by Voss et.al. (2014) [5] and Midttveit (2012) [22].

2.2 Characterization

Characterization of catalyst is a collective term for a wide range of tests for the physical and chemical properties of a catalyst. This section describes the theory and principles behind the characterization methods used in the thesis.

2.2.1 X-Ray Diffraction

X-Ray Diffraction (XRD) is a method to identify crystalline phases in a sample by analysing interference patterns of reflected X-rays. The sample is irradiated by X-Rays. The reflections of waves that hit a periodic lattice structure will form a constructive interference pattern, as illustrated in figure 2.2. The relation between reflection angle and lattice plane distance is described by Bragg's law (2.4) [1],

$$n\lambda = 2d\sin\theta \ ; \ n = 1, 2, ... \tag{2.4}$$

where λ is the X-ray wavelength, d is the distance between lattice planes, θ is the angle between the reflected wave and the normal plane, and n is the order of reflection.

The scattered X-Rays are registered, and the intensity of reflections that correlate to Bragg's law is plotted against angle to construct a XRD-pattern, also known as a diffractogram.

Crystalline compounds have characteristic diffraction patterns corresponding to their crystalline phase, making XRD a useful method for determining the crystalline phases of an unknown sample. The Scherrer-equation (2.5) relates the width of a peak in an XRD-pattern to the size of the crystalline particle.

$$< L >= \frac{K\lambda}{\beta\cos\theta} \tag{2.5}$$

Assuming a spherical particle, $< L >$ is the average crystallite diameter, β the peak width and K a constant regarded to be close to 1 [1, p. 133].

2.2.2 X-Ray Fluorescense

X-Ray Fluorescense (XRF) is a way to determine the mass composition of an oxide powder, metal or solutions. X-Rays of homogenous wavelength are scattered across a sample. The radiation excites electrons due to the photoelectric

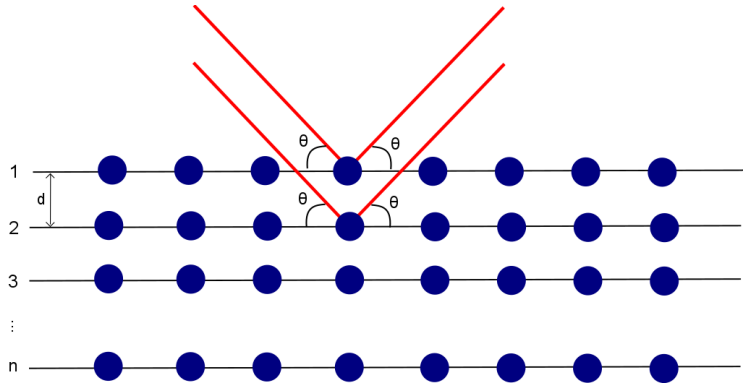

Figure 2.2: Illustration of how EM-waves are scattered by a periodical lattice. The red lines indicate the constructive interference pattern with a reflection angle θ on the lattice plane

effect. When the electrons relaxes, a photon is emitted with an energy corresponding to the energy potential between the relaxed and excited state. As elements have characteristic emission spectra, the elemental atoms of a sample may be determined by registering the wavelengths of the emitted radiation. The incoming wavelengths are determined by reflecting the radiation from the sample on a crystal and by detecting the scattering angle θ. Ordinary XRF-apparatus is only able to detect the elements in a certain range in the periodic table [23]. The Supermini2000, which has been used in this project, is able to detect elements between Fluorine and Uranium. As Oxygen is outside of this range the oxidation state of a compound can not be determined by XRF and must be determined in some other way (e.g. by XRD) in order to accurately determine the composition of a sample.

2.2.3 BET physisorption

Gas molecules can be physisorbed on a surface to measure surface area. Physisorption is a term for weak bonding (van der Waal-interaction) between a molecule and a surface. An adsorption isotherm curve may be obtained by plotting the adsorbed gas volume against pressure. Assuming that the surface is homogeneous, i.e. there is no local difference in adsorption enthalpy, the gas will adsorb in monolayers, completely covering the surface before starting a new

layer [24]. Nitrogen is commonly used for these purposes, as it is cheap, inert and has well characterized adsorptive properties.

Different materials may produce different isotherms. Microporous materials, such as zeolites, have too small pore diameters to facilitate unrestricted forming of multilayers. Capillary condensation leads to complete pore filling instead. This effect typically produces an IUPAC Type I adsorption isotherm (Figure 2.3) [1, p. 189-190].

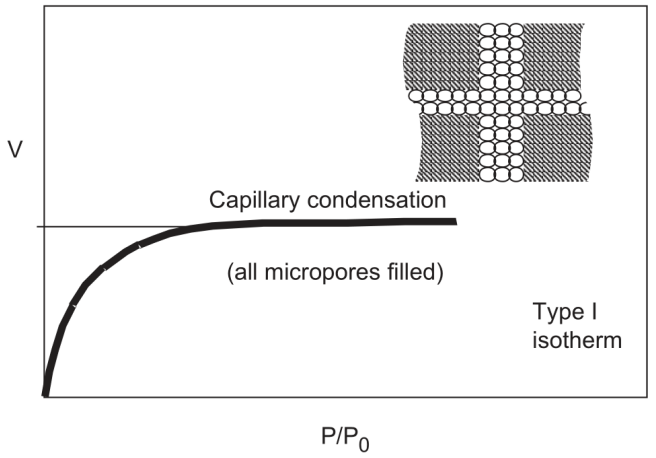

Figure 2.3: Representation of typical IUPAC Type I adsorption isotherm. Typical adsorption pattern for microporous materials. [1, p. 190].

Mesoporous materials will typically form an adsorption monolayer before it forms multilayers. Until the monolayer is formed, the isotherm resembles the Langmuir isotherm. At pore filling, the desorption will take place at lower pressures than adsorption, due to capillary condensation counteracting the driving force for desorption. This effect produces a characteristic hysteresis in the isotherm, classified as a IUPAC Type IV isotherm (Figure 2.4) [7]. Such isotherms are typical for materials like alumina and silica [1, p. 190].

As a molecule approaches a surface, the change of adsorption enthalpy increases rapidly close to the surface. It can be assumed that the adsorption of the first monolayer is stronger than physisorption in the second and higher monolayers. The adsorption enthalpy of higher monolayers are assumed to be the same, as the difference between them is small compared to the first. By also assuming

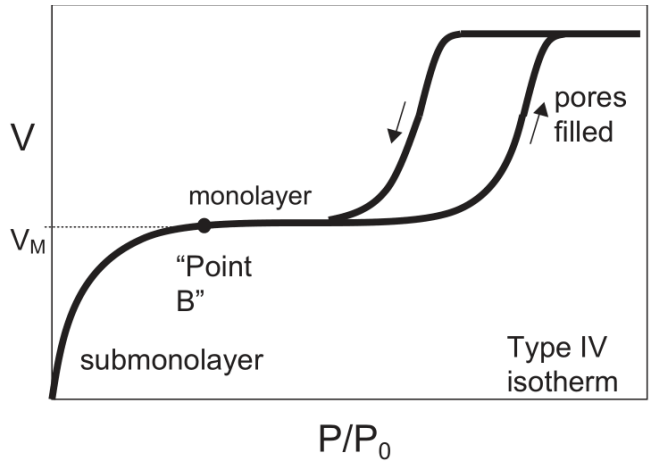

Figure 2.4: Representation of typical IUPAC Type IV adsorption isotherm. Typical adsorption pattern for mesoporous materials. [1, p. 190].

that the rate of adsorption and desorption is equal for all layers, The Braunauer, Emmet, Teller (BET) isotherm (2.6) may be derived [1, p.185-187],

$$\frac{P}{V_a\,(P_0 - P)} = \frac{1}{\chi V_0} + \frac{\chi - 1}{\chi V_0}\frac{P}{P_0} \equiv \eta + \alpha\frac{P}{P_0} \tag{2.6}$$

where P is the adsorption pressure, P_0 the equillibrium pressure of the condensed gas, V_a the total adsorbed gas volume, χ is the ratio of the desorption rate constants for the first and second monolayers, and V_0 the volume adsorbed in the first monolayer.

Plotting $\frac{P}{V_a(P_0-P)}$ against $\frac{P}{P_0}$ yields a linear plot with slope $\alpha = \frac{\chi-1}{\chi V_0}$ and y-axis intercept $\eta = \frac{1}{\chi V_0}$. By rearranging these terms, the volume of gas adsorbed in the first monolayer V_0 may be found as $V_0 = \frac{1}{\alpha+\eta}$. The ideal gas law may then be used to determine the amount of molecules, N_0, adsorbed in the first monolayer. If the surface area occupied by one N_2-molecule is known, the total surface area may be found by multiplying with the number of adsorbed molecules in the first monolayer [1].

Due to capillary condensation, gas may not necessarily desorb at the same pressure as adsorption as the capillary forces will have to be overcome. This phe-

nomenon is described by the Kelvin equation (2.7) [21, p. 262]:

$$\ln\left(\frac{P}{P_0}\right) = -\frac{2\sigma\bar{V}\cos\theta}{rRT} \tag{2.7}$$

where σ is the surface tension of the adsorbant (liquid nitrogen), $\bar{V}$ the molar volume of liquid nitrogen, θ the contact angle, between liquid and surface, r the pore radius, R the universal gas constant, and T the temperature.

The Barrett, Joyner, Halenda (BJH)-method is a way of determining the pore size and pore size distribution by relating BET multilayer adsorption to capillary condensation phenomena [25]. Due to capillary condensation phenomena, the desorption pressure is dependant on the pore radius (2.7). The adsorbed multilayer has a certain thickness at a given pressure P/P_0, which may be empirically determined. By relating the desorbed volume of gas at a pressure P/P_0 to capillary condensation and the adsorbant thickness, the pore size distribution of the support may be determined.

The method assumes that pores are cylindrical, and that the adsorbate in the pores only is affected by forces of physical adsorption on the pore wall and capillary condensation in the pore volume [25].

2.2.4 Infrared Spectroscopy

Infrared Spectroscopy (IR-spectroscopy) is a much used analysis technique capable of identifying molecules based on their vibrational energies. Within the field of catalysis it is commonly used to identify adsorbed species on a catalyst, and how they are chemisorbed to the catalyst [1, p. 155].

According to the Bohr model, atoms exists in discrete energy levels. In order to go from one state of energy to another, the atom must absorb a quanta of energy exactly to the difference of energy between the two levels. Electromagnetic radiation may be regarded as a stream of particles, *photons*, where the energy (E) of the photon is a product of it's frequency (ν) and the Planck constant ($h = 6.626 \times 10^{-34}$ J s), as described by the Bohr equation (2.8) [26, chap. 1].

$$E = h\nu \tag{2.8}$$

The same principle is applied to molecular vibrations or rotations. A transition between two vibrational mode may be seen as a transition between energy levels

and may occur if electromagnetic radiation of the right frequency is absorbed by an atom. Molecules can be identified by their characteristic absorption spectrum [26, 27].

Within the field of IR-spectroscopy, it is common to use the *wavenumber* ($\bar{\nu}$ [cm^{-1}]) instead of frequency or wavelength (λ). The relation between wavenumber, frequency and wavelength is shown in equation (2.9) [26].

$$\bar{\nu} = \frac{1}{\lambda} = \frac{\nu}{c} \tag{2.9}$$

Photons in the infrared spectrum that are absorbed cause transitions of vibrational energy in the molecule [28]. IR-spectroscopy exploits this phenomena by examining which wavelengths are absorbed in a sample. The vibrational energy transitions for various bonds, and thus the corresponding photon wavelengths can be predicted by quantum mechanical models [29, sec. 8.2], and used to identify species or functional groups.

DRIFTS spectra are commonly presented in the form of Kubelka-Munk units, especially for analysis of powders. The Kubelka-Munk equation (2.10) relates sample concentration to radiation intensity,

$$\frac{(1-R)^2}{2R} = \frac{c}{k} \tag{2.10}$$

where R is the absolute reflectance of the layer, c the sample concentration and k the molar absorption coefficient. [26, sec.2.5.3].

IR Spectroscopy may be used to determine the strength, type and number of acidic sites on a material. Acidity is commonly divided into two types, Brønsted and Lewis. Brønsted acids are defined as proton donoring molecules, whereas Lewis acids are defined as electron accepting molecules [15, chap. 4]. In solids (e.g. metal oxides) Brønsted acidic sites are usually present as surface OH-groups with loosely bound Hydrogen. Lewis acidic sites will form bonds to nucleophilic molecules [30].

If a basic probe molecule is adsorbed on the sample, the bond with the surface will impact the vibrational freedom of the basic molecule. The impact on the molecule is dependent on the type of bond, which creates characteristic bands in the IR-spectrum for different bonds. These may be analyzed further to determine bond strength and acidic site density [30]. The bond strength and distance

indicates the strength of the acid site, the number of acidic sites can be determined based on band intensity, and the type of acidic sites can be determined by the type of bond that is formed.

The IR spectrum of the pyridine vibrations most relevant for acid site characterization has been investigated by Parry (1963) [31]. The bands associated with pyridine adsorption are presented in table 2.1. The bands for Hydrogen-bonded pyridine and coordinatively bonded pyridine (Lewis acidic) are in general close to each other or are overlapping with each other. Brønsted active acidic sites will exchange a proton with the pyridine and form a pyridinium ion. The prescence of a pyridinium ion may be determined from vibrations at 1540 cm^{-1}, which is related to $N^+ - H$ bending.

Table 2.1: IR bands of pyridine (Py), and expected band intensity in the 1400-1700 cm^{-1} region, as reported by Parry (1963) [31]. The limits between H-bonded and coordinated Py were reported to not be well defined. Some fields in the table are intentionally left open to more easily compare bands in different columns. Intensities are abbreviated as follows: v.s.: very strong, s.: strong, m.: medium, w.: weak, v.: variable.

H-bonded Py	**Coordinatively bonded Py**	**Pyridinium ion**
1440-1447 (v.s.)	1447-1460 (v.s.)	
1485-1490 (w.)	1488-1503 (v.)	1485-1500 (v.s.)
		1540 (s.)
1580-1600 (s.)	$\approx$ 1580 (v.)	
	1600-1633 (s.)	$\approx$ 1620 (s.)
		$\approx$ 1640 (s.)

2.2.5 Scanning Electron Microscopy (SEM)

Electron microscopy is a common application for studying crystals, nanostructures and other materials at micro- and nanolevel. An electron microscope is in principal similar to it's optical counterpart, but uses a high energy beam of electrons instead of light to generate a signal. The low wavelength of electrons makes very high resolution at high magnification possible. The high energy electron beam causes several physical effects on the sample, which may be analysed to obtain information about a.o. surface topology/structure, composition, dispersion of elements. The primary sources of information used to construct

an image are Backscattered Electrons (BSE), Secondary Electrons (SE) and emitted X-Rays.

The volume of the sample affected by the electron beam is commonly referred to as the *interaction volume*. This volume is drop shaped, as the signal is increasingly scattered as it penetrates deeper into the sample. The penetration depth and width of the interaction volume depends on the beam voltage and current, as well as the material of the sample being examined.

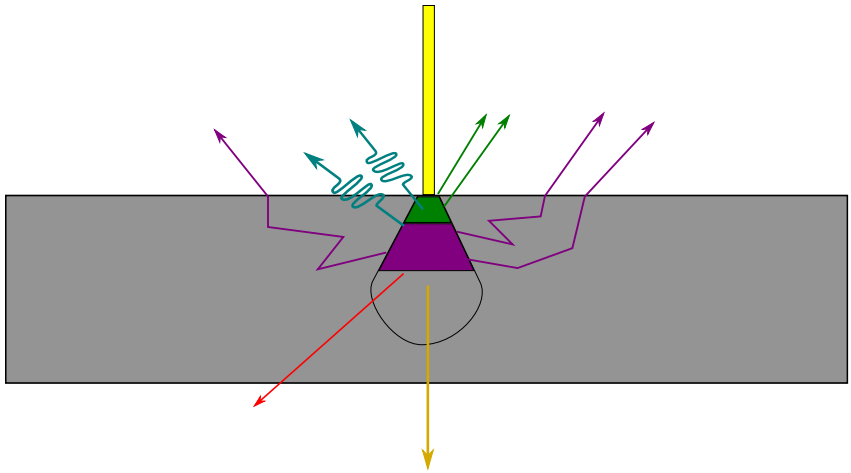

Figure 2.5: An illustration of the different signals generated at various depth in a sample during S(T)EM. The primary electron beam (yellow) causes a range of physical phenomena in the sample, and affects the sample in a dropshaped volume. Different signals arise from different depths, amongst them: Secondary Electrons (green) close to the surface, X-Ray radiation (Blue), Backscattered Electrons (purple), diffracted electrons (red) and Transmitted Electrons (gold).

Backscattered Electrons are high-energy electrons that goes through several inelastic collision in the sample during which they are scattered back towards

the sample surface. Larger atoms will be more likely to backscatter electrons than smaller atoms. [32, p.75-76] An effect of this is elemental contrast between heavier elements and smaller elements that may indicate the dispersion of heavy elements in a sample. BSE may not determine the element precisely, but indicates where heavy atoms are located relative to the "background" [29, p.169]. Backscattered electrons penetrate deeper into the sample than Secondary electrons, and can provide information from below the surface region of the sample.

Electrons in the outer shells of an atom may be set in motion by colliding electrons, either backscattered or from the primary beam. Such electrons are classified as Secondary Electrons (SE), and has lower energy than backscattered electrons [32, p.89-90]. There is a certain probability that a secondary electron will collide with an atom before it "escapes" from the specimen surface. As the chance of collision is smaller close to the surface of the sample, most of the secondary electrons provide information of the shallowest region of the interaction volume of the sample [29, p. 169-170], marked in green in Figure 2.5.

Electrons, like photons carry a specific quanta of energy. As mentioned in section 2.2.2, an energy quant may excite atoms to a higher energy state. The excited atom may then emit energy in form of a photon to relax to it's original lower energy state. The emitted radiation is characteristic for the atoms. Elemental mapping, i.e. determining the location of specific elements in the sample, is therefore possible by analyzing the emitted radiation from the sample. These signals may be detected and analysed by Energy-dispersive X-ray spectroscopy (EDX).

The primary electron beam delivers a continuous stream of electrons to a small part of the sample. These electrons are usually led away from the surface by the material or as SE or BSE. Electric isolators may not be able to lead electrons to ground as fast as the beam delivers them, leading to an accumulation of electrons at the incident spot. This phenomenon is usually called *charging* [33, p.247-250] and will distort the signal generation. The effect of charging on SEM imagery may vary from small bright spots, to distortions of a large areas [33, p.251].

Chapter 3

Methods

Procedures, operating conditions, equipment and other parameters for experimental work performed for the thesis is described in the following chapter. Section 3.1 outlines the procedure for preparation of the catalysts that were analysed, while section 3.2 describes the procedures for the various methods used to characterize the catalysts.

3.1 Preparation of Ordered Mesoporous Alumina and HPW-Alumina composites

Mesoporous Al_2O_3 was prepared by the sol-gel method, based on a procedure described by Armatas et.al (2010) [6]. A sol containing an Al-precursor (Aluminum isopropoxide, $Al(OPr)_3$) and a surfactant (Pluronic F127) was prepared. 2.04 g $Al(OPr)_3$ was dissolved in 10 mL ethanol (absolute) and 1.0 mL HNO_3 (70%). Separately, approximately 1 gram of Pluronic F127 was dissolved in 10 mL ethanol (absolute) and 0.5 mL HNO_3 (70%). Appropriate amounts (0.17 g and 0.60 g for 25% and 50% respectively [1]) of solid HPW was dissolved in 1.5 mL of ethanol (absolute).

The solutions containing $Al(OPr)_3$ and F127 was mixed and stirred rigorously for five minutes. The HPW solution was added dropwise after the initial stirring for HPW-samples. The sol was then left to stir for 4 hours in room temperature.

After 4 hours of stirring in room temperature, the sol was aged for three days at 60 °C. The xerogel was calcined at 400 °C under flowing air with a temperature ramp rate of $0.5°C\,min^{-1}$. Calcination time for each sample is shown in Table 3.1.

Table 3.1: List of samples of HPW-mesoporous alumina, detailing mass percentage of HPW and calcination time. All samples were calcined at 400 °C.

Sample name	**HPW [%]**	**Calcination time [h]**
m-Al_2O_3_1	-	4.0
m-Al_2O_3_2	-	4.0
m-Al_2O_3_3	-	4.0
25HPW-Al_2O_3_1	25	4.0
50HPW-Al_2O_3_1	50	8.0
50HPW-Al_2O_4_2	50	4.0

[1] see appendix A.1 for calculation of HPW precursor mass

3.2 Characterization

The catalysts were characterized by XRD, XRF, BET Physisorption, S(T)EM and FTIR spectroscopy. Parameters, procedures and analysis conditions are presented in subsections for each method.

3.2.1 X-Ray Diffraction

XRD was used to determine crystallinity and potential crystallic phase of Al_2O_3. XRD-analyses were performed on powder samples by a Bruker D8 Advance DaVinci instrument with a Copper-anode and wavelength $\lambda = 1.54$ Å, 0.1° divergence slit at 2θ between 5° and 75°.

Small Angle analyses was performed at angles $\theta = [1.2 : 40]$, 0.005° divergence slit and 0.11° PSD opening for 60 minutes with 12.6 seconds per step.

In an attempt to obtain diffractograms of a dehydrated surface of the HPW-containing samples, diffractograms og 25HPW1 and pure HPW was obtained. The samples were first heated at 110°C before being placed in an airtight XRD sample holder and analyzed with a D8-Focus diffractometer with a Copper-anode and wavelength $\lambda = 1.54$ Å, 1.0 mm divergence slit at 2θ between 5° and 75° and 0.3 seconds per step.

The obtained data was processed and analyzed by Diffrac.Eva analysis suite.

3.2.2 X-Ray Fluorescence (XRF)

X-Ray Flourescence (XRF) was used for elemental analysis of the alumina-HPW composites. Approximately 200 mg catalyst and 2.5-3 g of a binder material (H_3BO_3) was mixed, grinded and pressed into a circular pellet. Samples were analyzed using a Supermini2000 XRF apparatus.

3.2.3 BET Physisorption

BET physisorption was performed using a Micromeritics TriStar II. Samples of approximately 0.1 g were set under vacuum at 200 °C overnight in order to desorb any adsorbed species in the sample. The samples were installed in the

machine, evacuated and cooled by liquid nitrogen to a temperature of -195 °C. Measurements were made with an equilibrium interval of 5 seconds.

3.2.4 IR-spectroscopy

IR spectroscopy was performed using a Nicolet iS50 FT-IR Spectrometer. The analytic procedures were based on those developed by Coucheron (2014) [34].

In situ DRIFTS measurements were performed using a Harrick Praying Mantis cell and a high temperature reaction chamber with KBr windows. N_2 was used to maintain a neutral atmosphere in the cell. Pyridine adsorption experiments were done by bubbling N_2 through pyridine. To facilitate this, the N_2-line was split upstream of the cell. A Process Flow Diagram (PFD) of the apparatus is presented in Figure 3.1. The praying mantis cell was heated by a Harrick ATC-024-4 Temperature controller, and water-cooled by an EHEIM 2217 Aquarium pump.

Samples were diluted to 1 wt% by solid KBr and crushed to a fine powder in a mortar. The sample holder in the cell was filled with the diluted samples, which were packed tight to obtain an as even surface as possible. N_2 (15 mL min^{-1}) was flowed through the cell at all times, except during pyridine adsorption. The cell was heated rapidly to 500 °C. Samples were held at this temperature for 1 hour to dehydroxylate the surface and remove any adsorbed species. The samples were then cooled to 150 °C. A single background spectrum was obtained and used as background for all following spectra. Pyridine vapor was then introduced to the cell by bubbling N_2 (30 mL min^{-1}) through liquid pyridine for 30 minutes. Spectra were recorded every minute from the point of pyridine introduction until the end of the experiment. The N_2-flow was switched to bypass the pyridine bubbler after 30 minutes, and set to flow over the cell at 15 mL min^{-1} for one hour, after which the experiment was ended.

Spectra were converted to Kubelka-Munk units by the Omnic software.

Fityk 0.9.8 was used as a peak fitting tool to deconvolve peaks. A Voigt peak shape was chosen for all peaks. The peaks were assigned according to the observed spectrum, and fitted by the software using the Levenberg-Marquardt method.

3.2.5 S(T)EM

Electron microscopy imaging was performed with a Hitachi S-5500 S(T)EM. Powder samples were crushed in a mortar and fastened to a sample stub using Carbon tape. High resolution images of pore structure and surface were obtained with a probe voltage V_{acc} between 2.0 and 5.0 kV and probe current A between 2.0 and 8.0 µA, depending on the sample and required magnification. EDX mapping was performed with an attached Bruker XFlash EDX Detector, and a typical V_{acc} of 10-15 kV and $A \simeq 10$ µA.

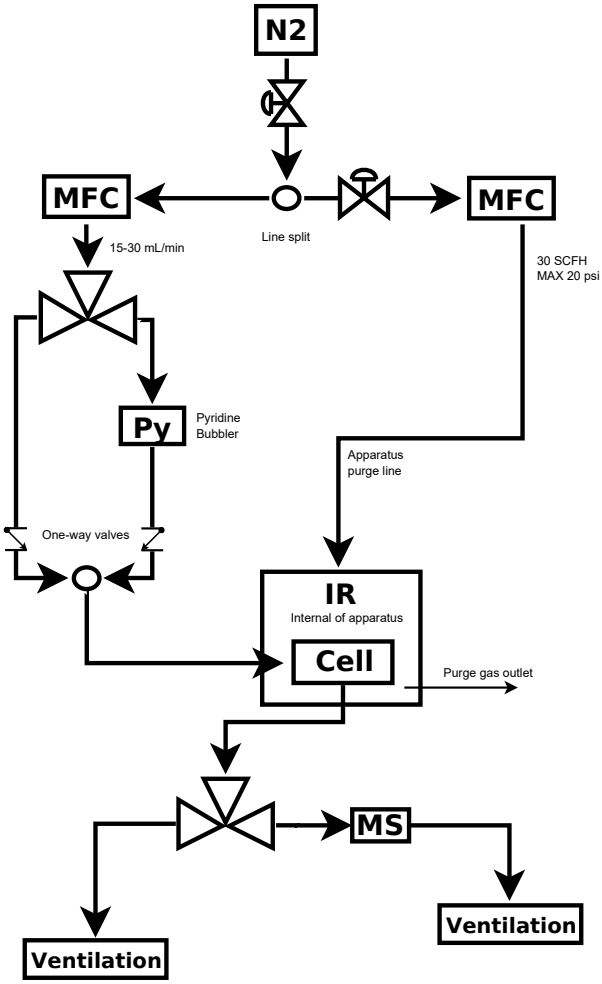

Figure 3.1: PFD of gas lines and instruments used in the IR-spectroscopy measurements. The N_2 can be routed directly to the sample, or be bubbled through a pyridine bubbler ("Py") before flowing to cell. Nitrogen is used as purge gas (the line labelled "Apparatus purge line") to avoid that air, dust or other contaminants disturb the generation of the IR signal. The purge gas does not come in contact with the sample in the cell. A Mass Spectrometer (MS) could be used to analyze the output from the cell.

Chapter 4

Results

Experimental results of characterization and and other analyses of the samples are presented in the following chapter. The results are organized in sections by method. All results are discussed in Chapter 5.

4.1 Characterization

Mesoporous aluminas and HPW-modified mesoporous aluminas were characterized by BET Physisorption, X-Ray Diffraction (XRD), X-Ray Fluorescence (XRF), S(T)EM and FTIR.

4.1.1 XRF

XRF was used to determine the elemental composition of HPW-modified aluminas. The results are presented in table 4.1.

Table 4.1: Results of XRF analysis of HPW-aluminas. As XRF is not able to determine oxides, the elemental composition is presented as the presumed oxide.

Sample	**Component**	**Mass Percentage [%]**
25HPW1		
	Al_2O_3	86
	WO_3	14
	P_2O_5	0.5
50HPW2		
	Al_2O_3	64
	WO_3	36
	P_2O_5	0.2

4.1.2 BET

BET-analysis was used to characterize pore size and surface area of the materials. Key BET results for all samples are presented in table 4.2. BET Isotherms and BJH pore distribution plots are plotted in Figures 4.1 to 4.14. The BET isotherms of 50HPW1 and 50HPW2 are compared in Figure 4.15 and Figure 4.16, respectively. BJH pore distributions for all samples are compared in Figure 4.17.

Table 4.2: Key BET parameters for mesoporous alumina samples. Average (Avg.) pore diameter and size are based on BJH Desorption results. The results reported for the sample named "γ-Al_2O_3" are the results of a commercial γ-Al_2O_3 analysed by BET during the specialization project prior to the Master project. All analyses were performed under the same parameters and conditions, as described in Section 3.2.3.

Sample	**BET Surface Area** [$m^2\,g^{-1}$]	**Avg. Pore Diameter** [nm]	**Avg. Pore Volume** [$cm^3\,g^{-1}$]
γ-Al_2O_3	137	20.4	0.70
m-Al_2O_3_1	309	3.8	0.36
m-Al_2O_3_2	300	7.5	0.46
m-Al_2O_3_3	286	4.1	0.36
25HPW-Al_2O_3_1	238	4.9	0.36
50HPW-Al_2O_3_1	127	4.4	0.17
50HPW-Al_2O_3_2	168	3.9	0.18

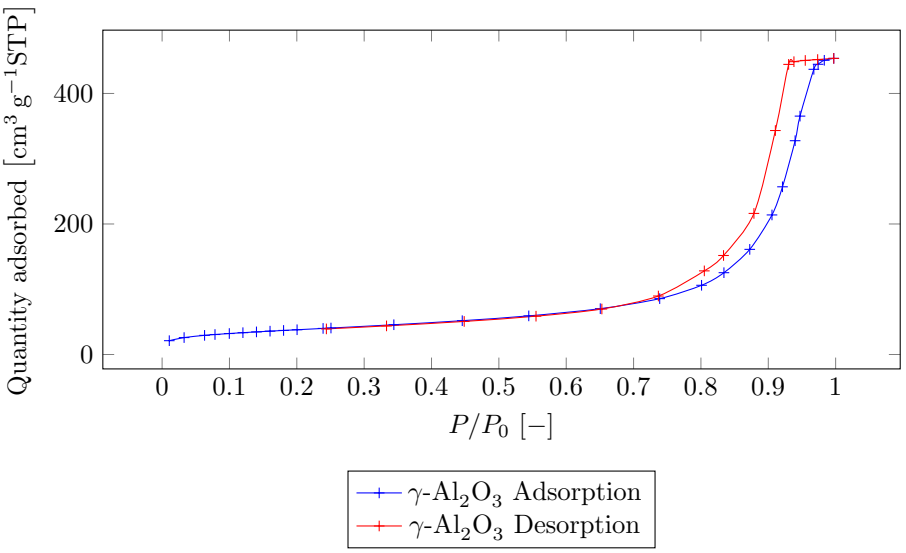

Figure 4.1: BET Isotherm of a commercial γ-Al_2O_3. The BET/BJH analysis was performed as part of the specialization project prior to the thesis work, with the same parameters and conditions as the other BET analyses presented in this section.

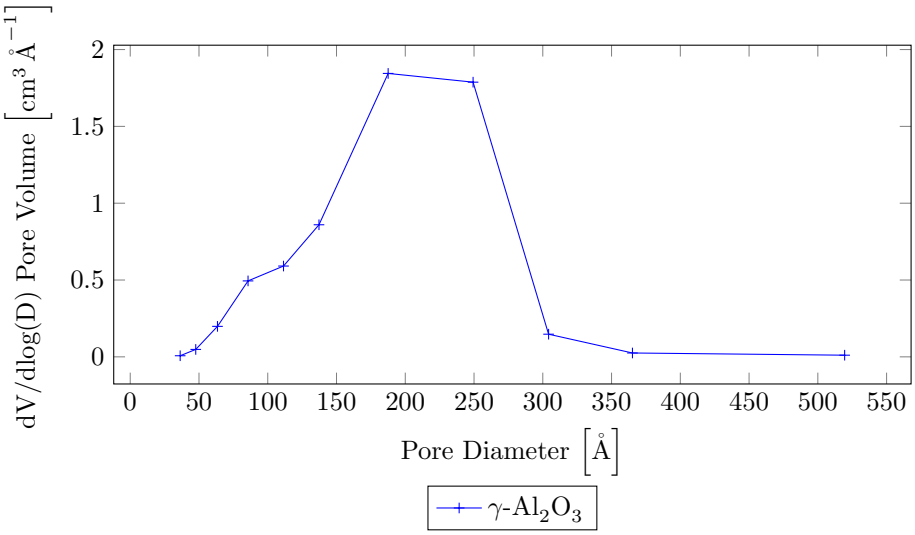

Figure 4.2: BJH Desorption analysis of a commercial γ-Al_2O_3. The BET/BJH analysis was performed as part of the specialization project prior to the thesis work, with the same parameters and conditions as the other BET/BJH analyses presented in this section.

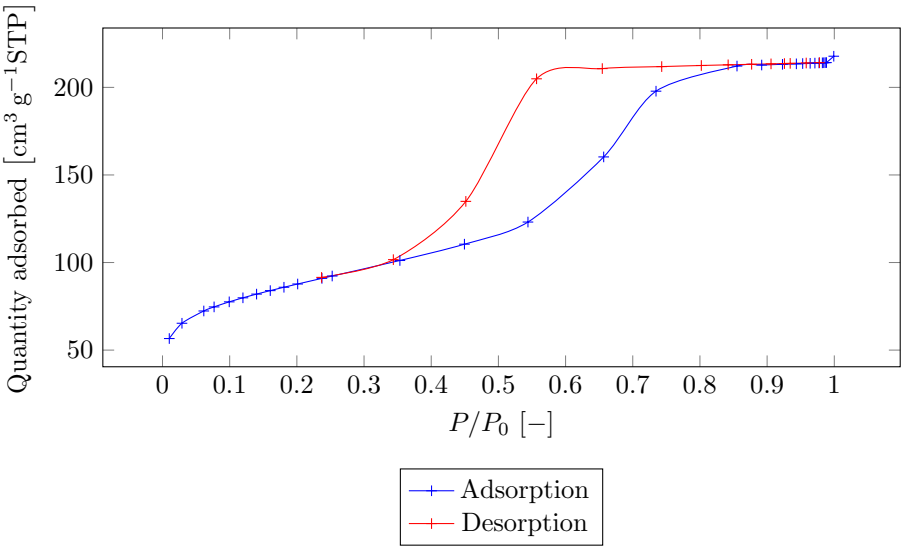

Figure 4.3: BET plot of m-Al_2O_3_1, showing the obtained isotherms for adsorption and desorption

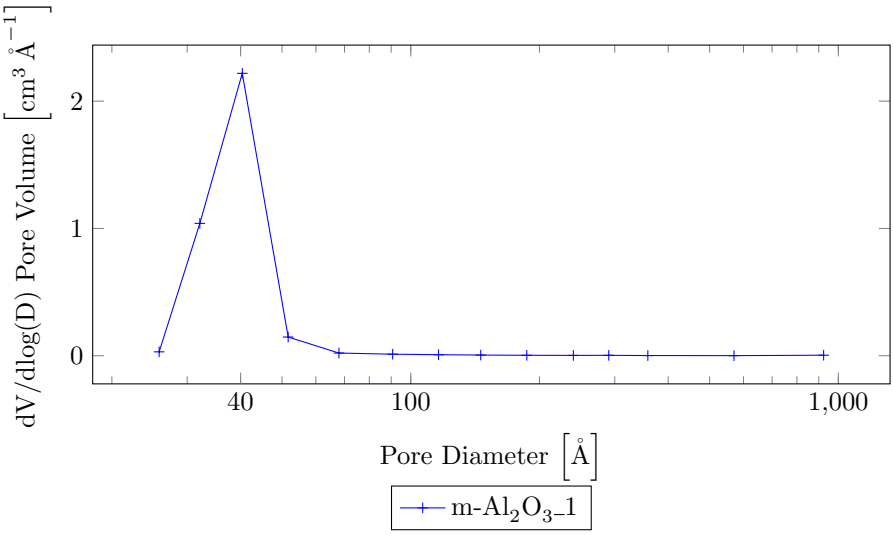

Figure 4.4: BJH Desporption of m-Al_2O_3–1, showing the distribution of pore volume for pore size. The X-values are plotted on a logarithmic scale.

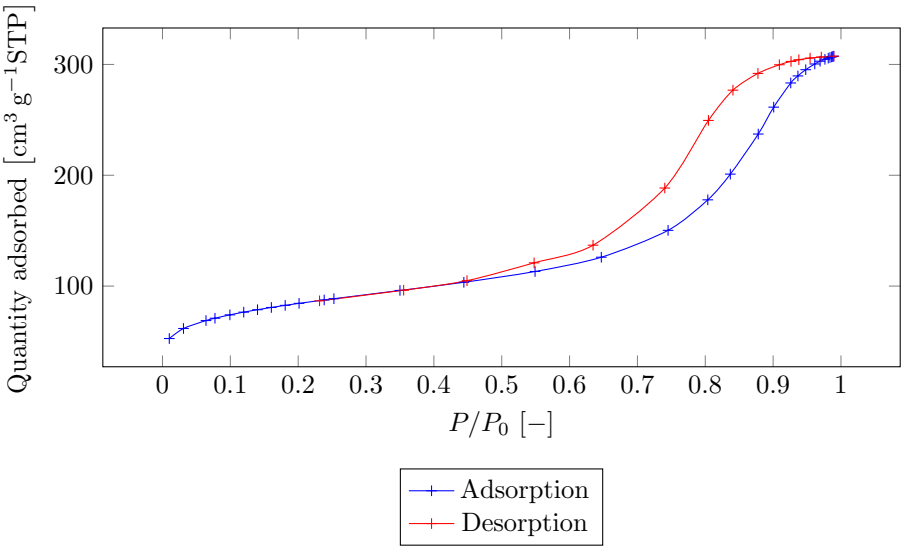

Figure 4.5: BET Isotherm of m-Al_2O_3_2, showing the obtained isotherms for adsorption and desorption.

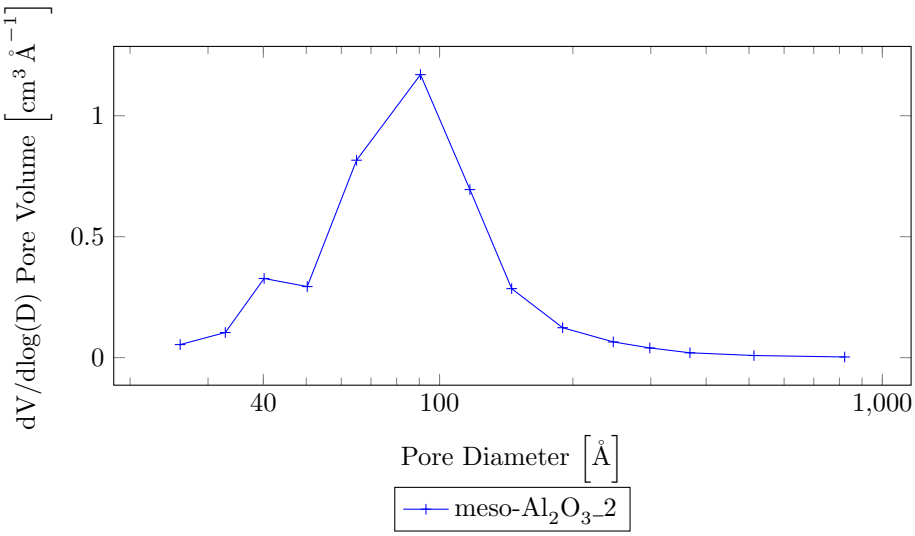

Figure 4.6: BJH Desporption of meso-Al_2O_3_2, showing the distribution of pore volume for pore size. The X-values are plotted on a logarithmic scale.

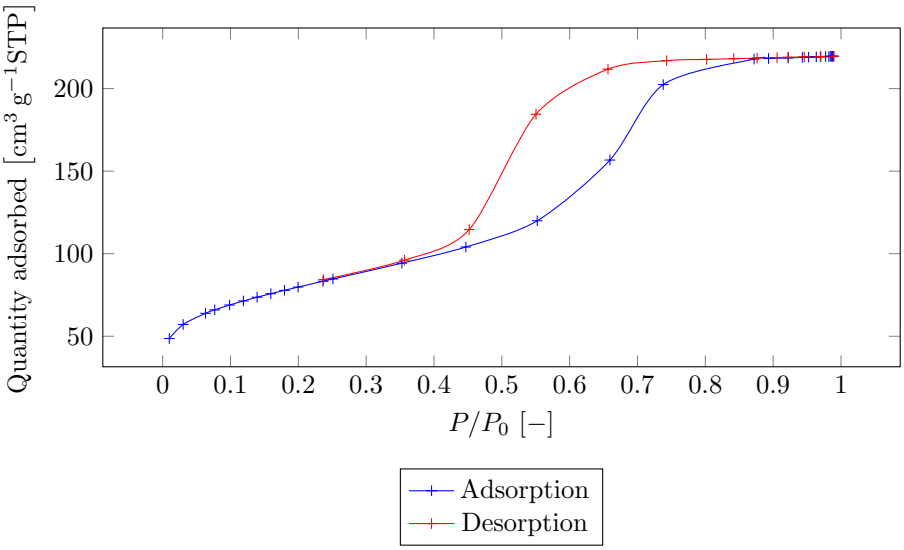

Figure 4.7: BET Isotherm of m-Al_2O_3_3, showing the obtained isotherms for adsorption and desorption.

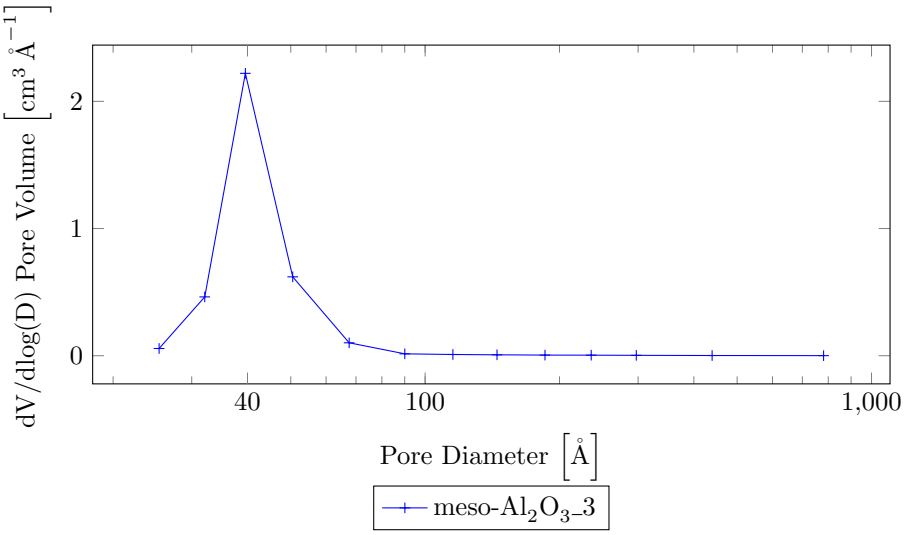

Figure 4.8: BJH Desporption of meso-Al_2O_3_3, showing the distribution of pore volume for pore size. The X-values are plotted on a logarithmic scale.

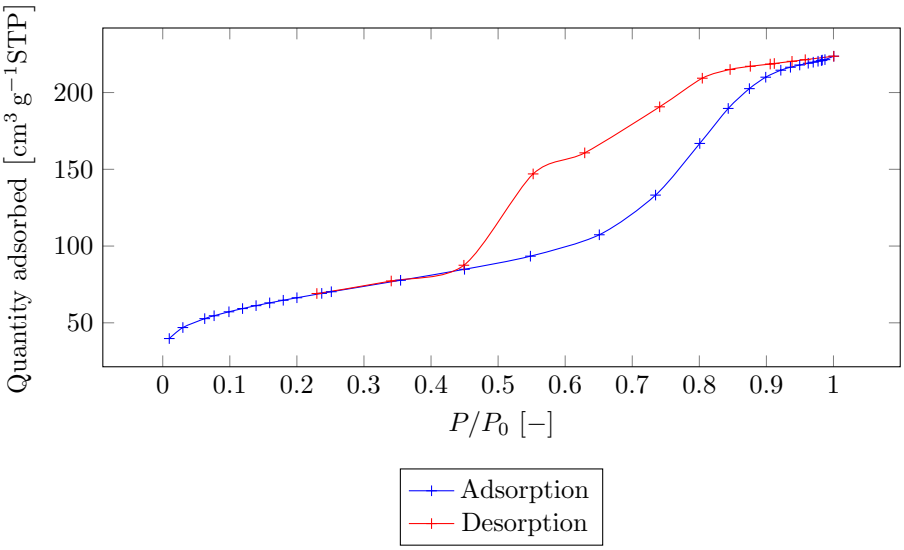

Figure 4.9: BET Isotherm of 25HPW, showing the obtained isotherms for adsorption and desorption.

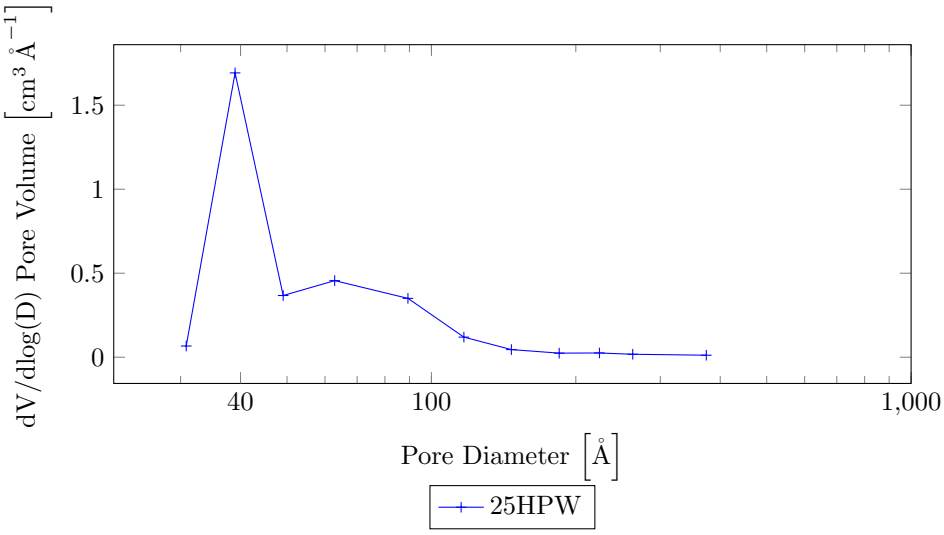

Figure 4.10: BJH desorption analysis of 25HPW, showing the distribution of pore volume for pore size. The X-values are plotted on a logarithmic scale.

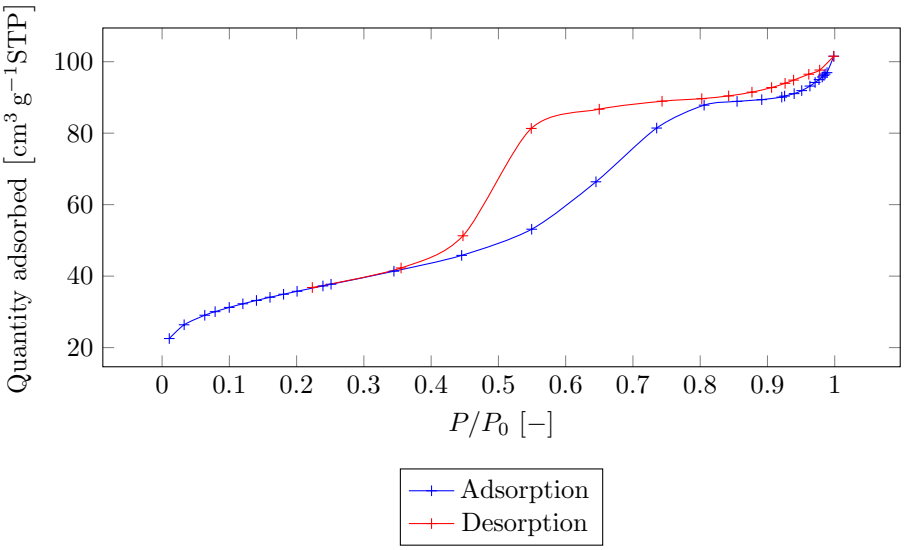

Figure 4.11: BET Isotherm of 50HPW1, showing the obtained isotherms for adsorption and desorption.

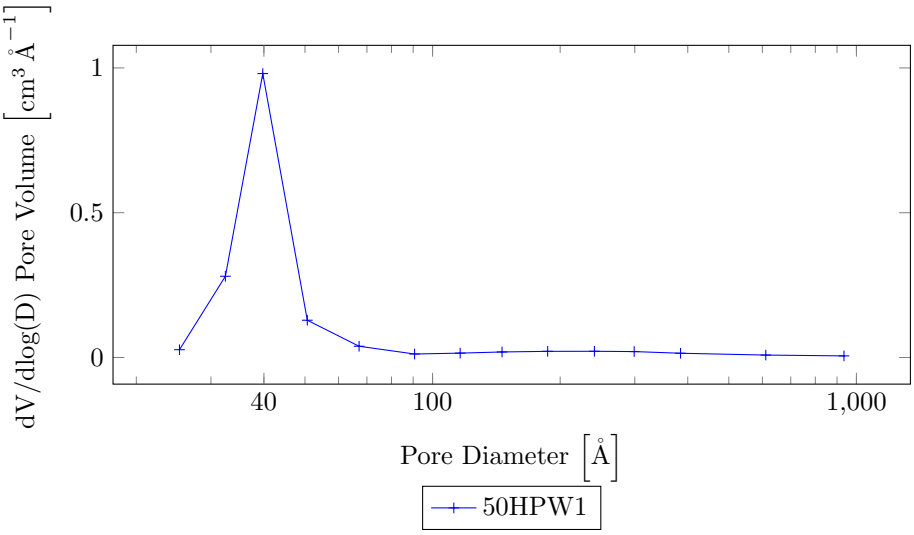

Figure 4.12: BJH desorption analysis of 50HPW1, showing the distribution of pore volume for pore size. The X-values are plotted on a logarithmic scale.

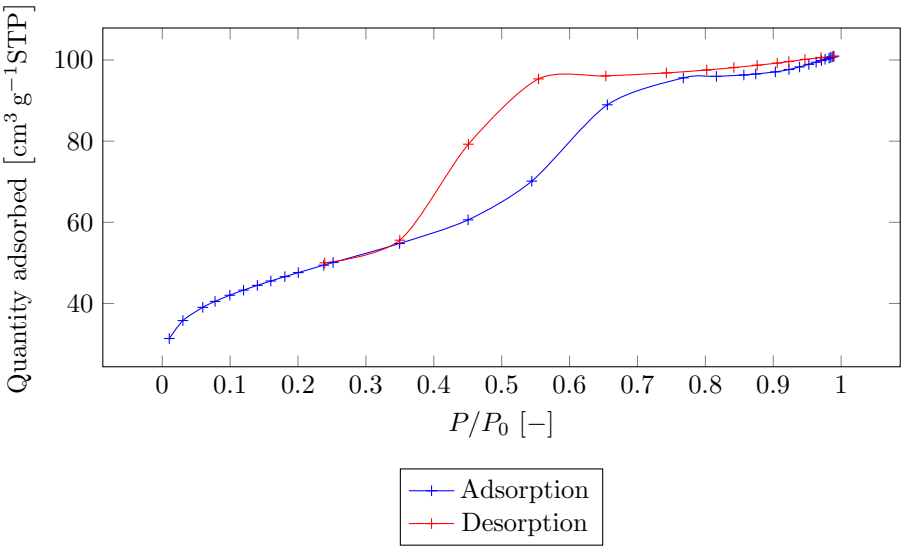

Figure 4.13: BET Isotherm of 50HPW2, showing the obtained isotherms for adsorption and desorption.

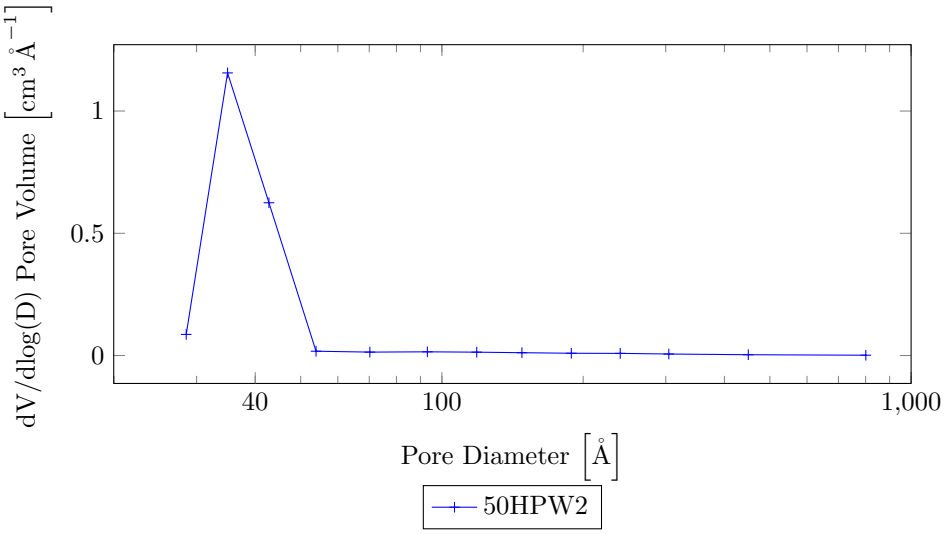

Figure 4.14: BJH desorption analysis of 50HPW2, showing the distribution of pore volume for pore size. The X-values are plotted on a logarithmic scale.

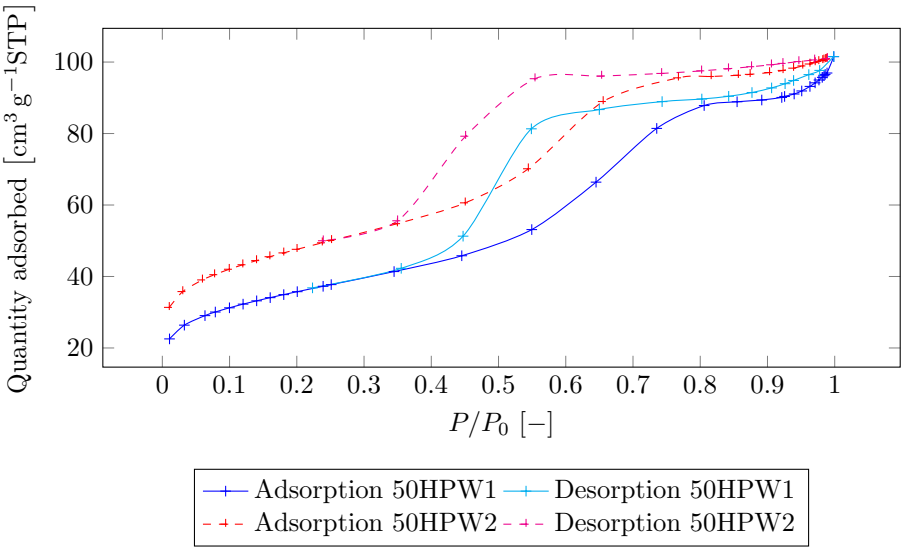

Figure 4.15: Comparison of BET Isotherms of both parallels of 50HPW.

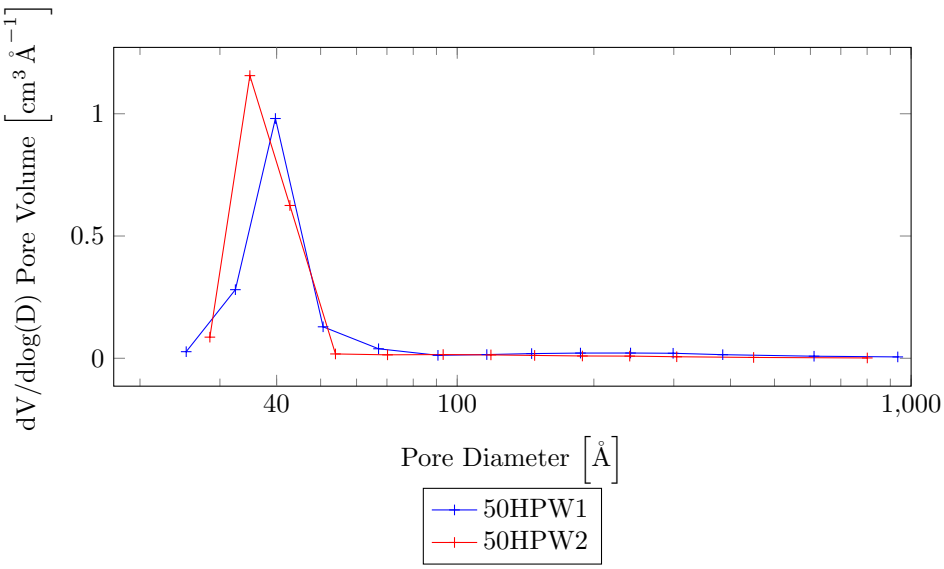

Figure 4.16: Comparison of pore distributions of 50HPW1 and 50HPW2. The X-values are plotted on a logarithmic scale.

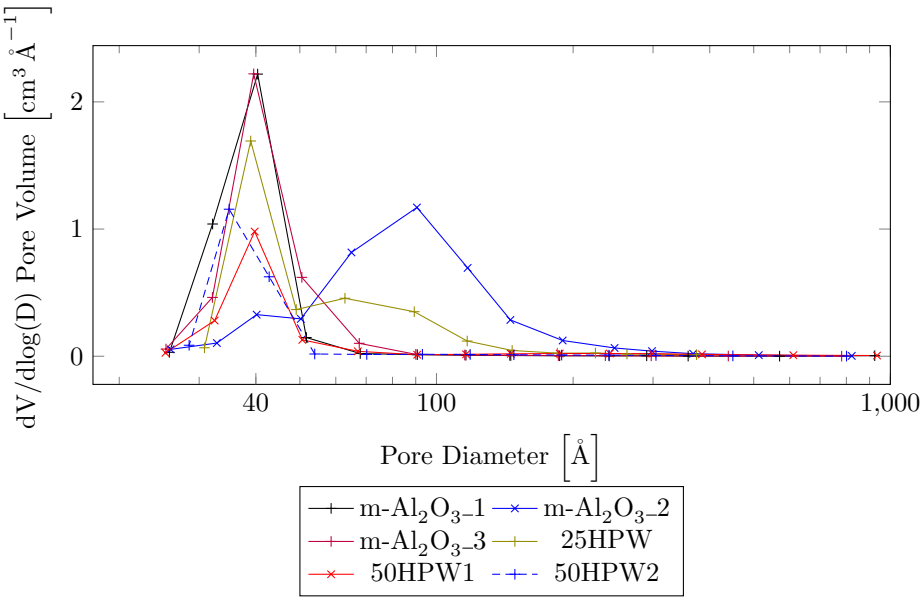

Figure 4.17: Comparison of BJH pore distributions plotted in previous figures for all samples. X-values are plotted on a logarithmic scale.

4.1.3 XRD

XRD diffractograms in figures 4.18, 4.19 were obtained using a DaVinci diffractometer at 2θ range 5-75, and $\lambda = 1.5406$ Å. Figure 4.21 is a Small Angle diffractogram obtained by a DaVinci diffractometer. The diffractograms in Figure 4.20 were obtained by using a D8 Focus diffractometer at. Parameters for the analyses are presented in Section 3.2.1.

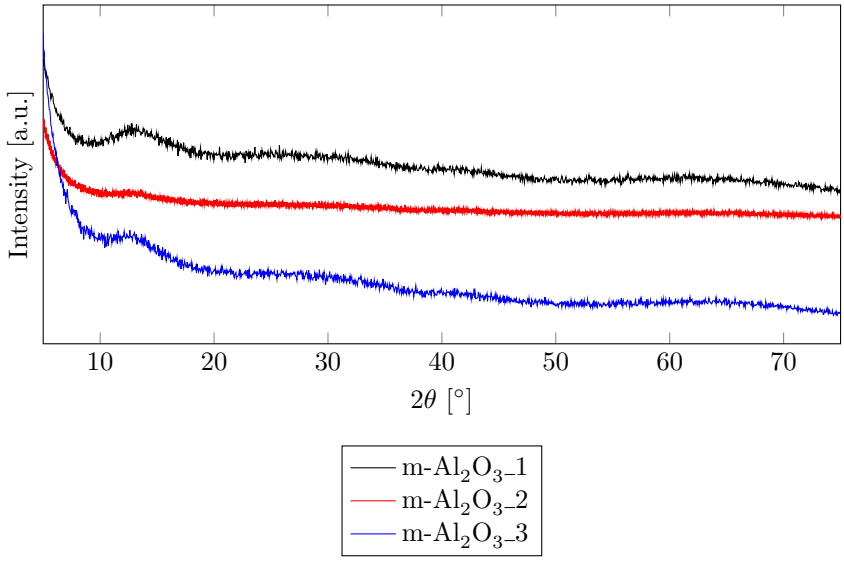

Figure 4.18: XRD Diffractogram of m-Al_2O_3_1, m-Al_2O_3_2, m-Al_2O_3_3, obtained by DaVinci Diffractometer. The graphs are plotted on an arbitrary Y-scale.

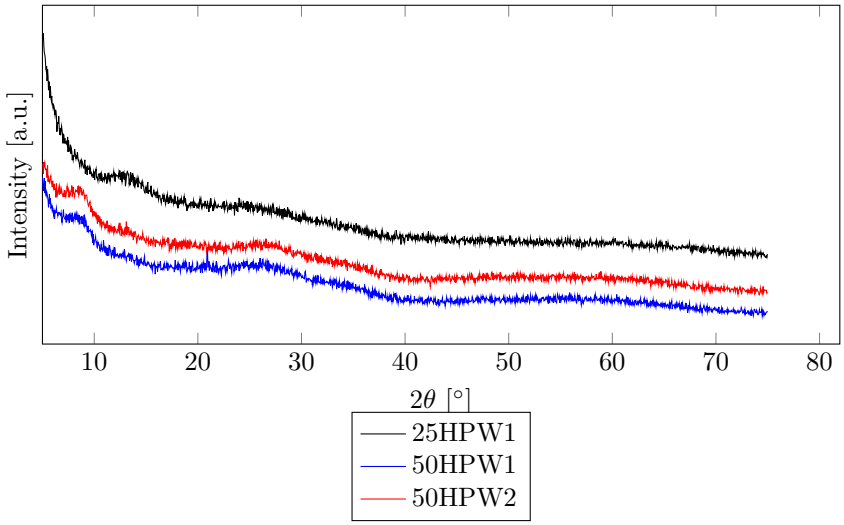

Figure 4.19: Diffractogram of 25HPW1, 50HPW1, 50HPW2, obtained by DaVinci Diffractometer. The graphs are plotted on an arbitrary Y-scale.

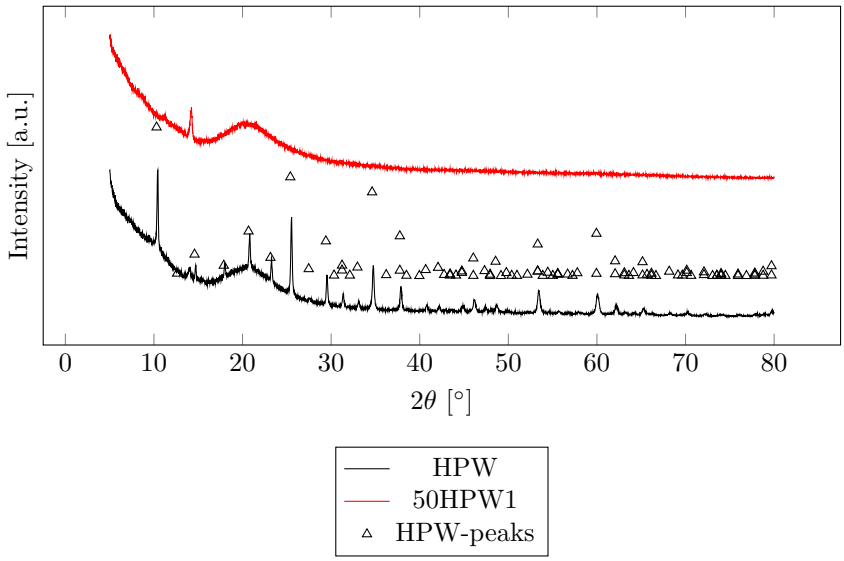

Figure 4.20: Comparison of Diffractograms for dehydrated HPW and 50HPW-alumina. Both samples were kept heated overnight at 110degreeCelsius before XRD was performed in an airtight container, using a D8 Focus Diffractometer. The coordinates for expected HPW-peaks were found in a Diffrac.EVA database. Graphs are plotted on an arbitrary Y-scale.

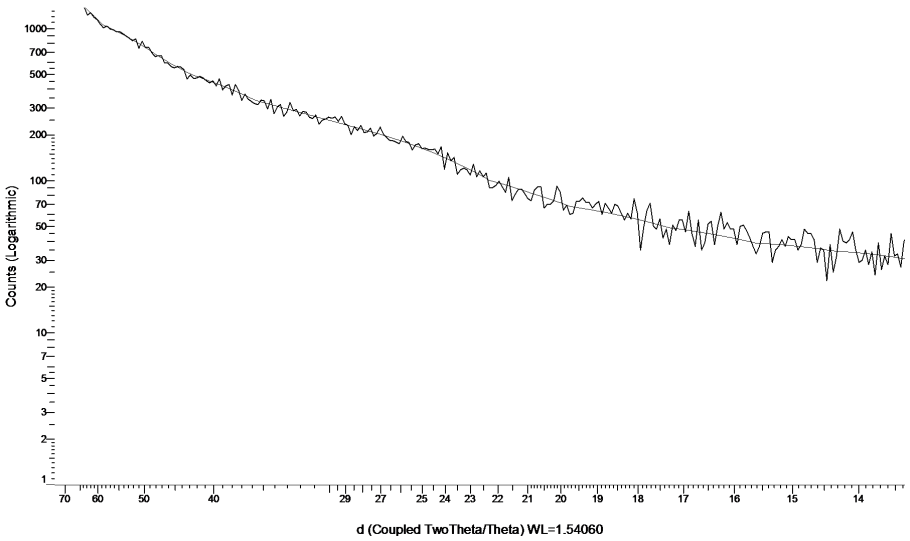

Figure 4.21: Small angle XRD results, obtained by analysing a m-Al_2O_3_1 sample at the parameters previously described. Angles in the range $\theta = [1.5, 50]$. The results are shown plotted for lattice place distance d. The relation between θ and d is shown in the Bragg equation (2.4).

4.1.4 FT-IR

Pyridine adsorption as a method for determining surface acidity of materials is an established method, studied by several authors. The analysis of bands and spectra, and assignment of peaks in this section is much based on the work of [27, 35–38]. IR-intensities are plotted in dimensionless Kubelka-Munk units.

Peak fitting was performed to deconvolve spectra. The centra of the most prevalent peaks found in the peak fitting is plotted with the spectra (Figure 4.22). A plot of peak area vs. peak center is presented in Figures 4.23 and 4.24.

Figures 4.25 to 4.28 show the pyridine adsorption spectra at several timepoints to show the saturation and desorption of pyridine.

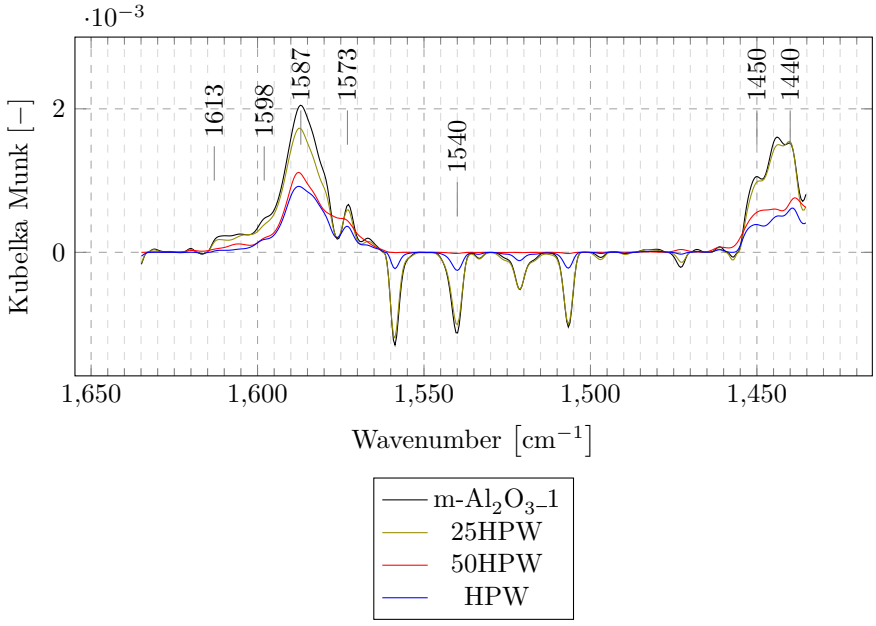

Figure 4.22: IR-spectrum of m-Al_2O_3, 50HPW and HPW in the wavenumber range of 1435-1635 cm^{-1} five minutes after the pyridine bubbling was ended. The spectra were taken at 150 °C under a flow of 15 mL min^{-1} N_2

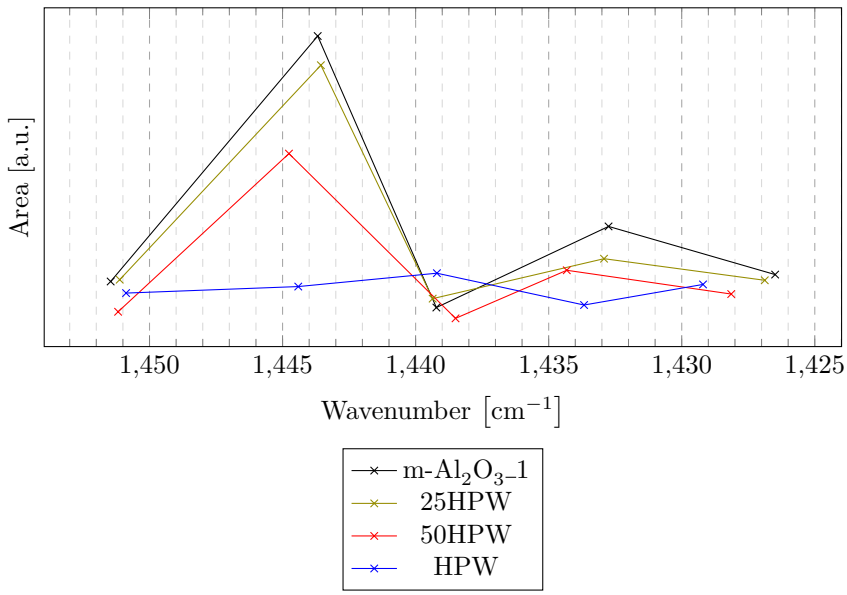

Figure 4.23: Comparison of the integrated area for peaks fitted by Fityk, in the region 1400:1470 cm^{-1}. The original spectrum is presented in Figure 4.22.

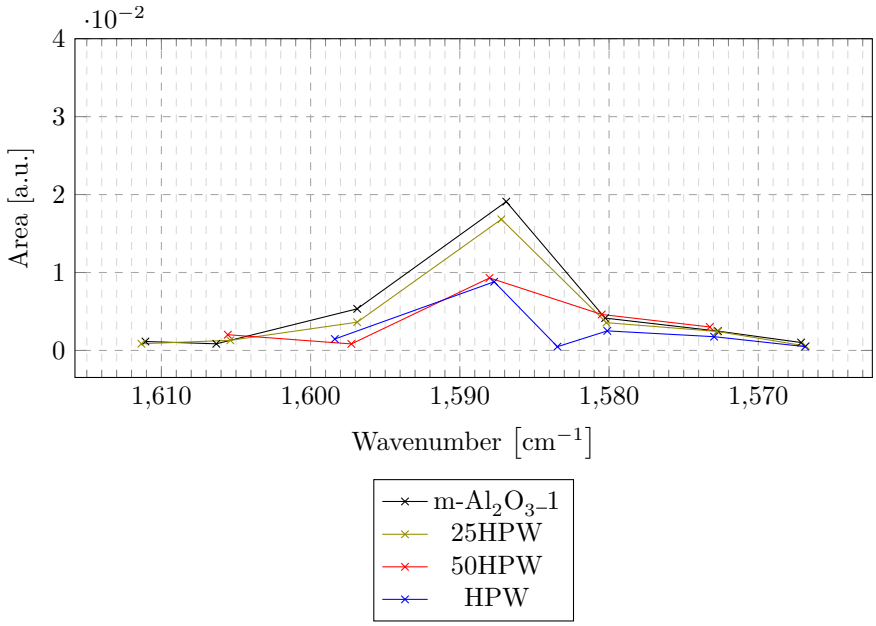

Figure 4.24: Comparison of the integrated area for peaks fitted by Fityk, in the region 1560:1620 cm^{-1}. The original spectrum is presented in Figure 4.22.

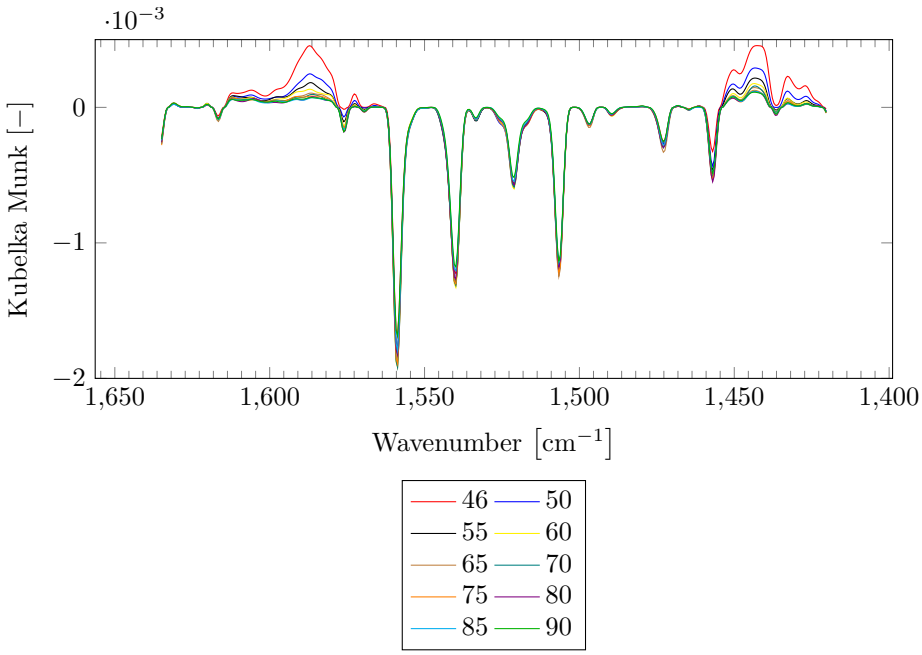

Figure 4.25: m-Al_2O_3_1: Desorption of pyridine, shown by plotting IR spectrums from 10 minutes after desorption was finished until the experiment was ended. The numbers given in the legend equals Time on Stream (TOS) in minutes. Pyridine was bubbled from TOS=6 to TOS=36 for this sample. After this point, N_2 was flowed through the cell to keep the conditions in the cell as stable as possible. The temperature was held constant at 150 °C at all times.

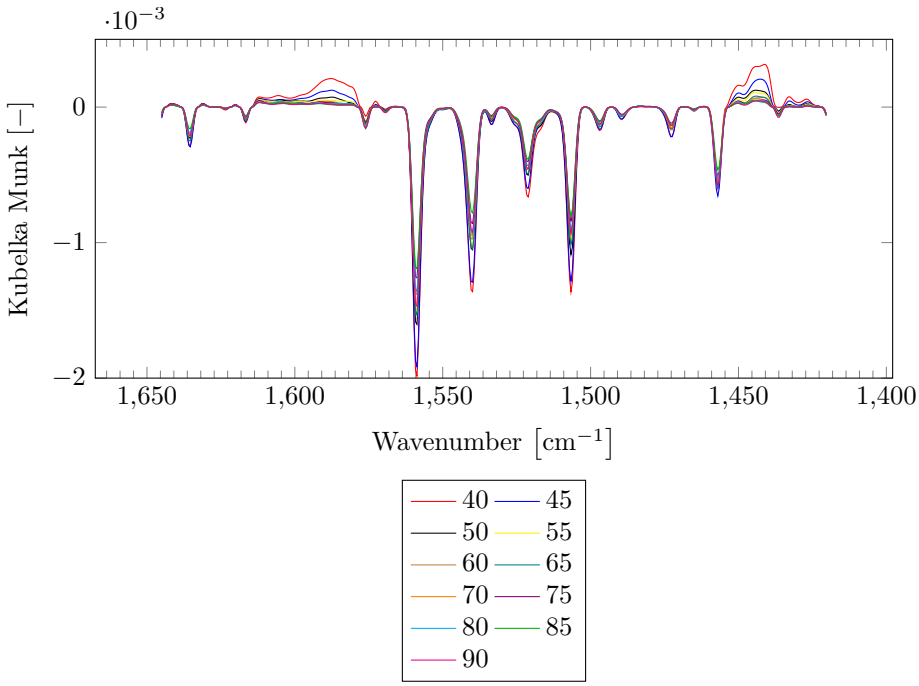

Figure 4.26: 25HPW: Desorption of pyridine, shown by plotting IR spectrums for different points of Time On Stream (TOS). The numbers given in the legend equals TOS in minutes. Pyridine was bubbled from TOS=1 to TOS=30. After this point, N_2 was flowed through the cell to keep the conditions in the cell as stable as possible. The temperature was held constant at 150 °C at all times.

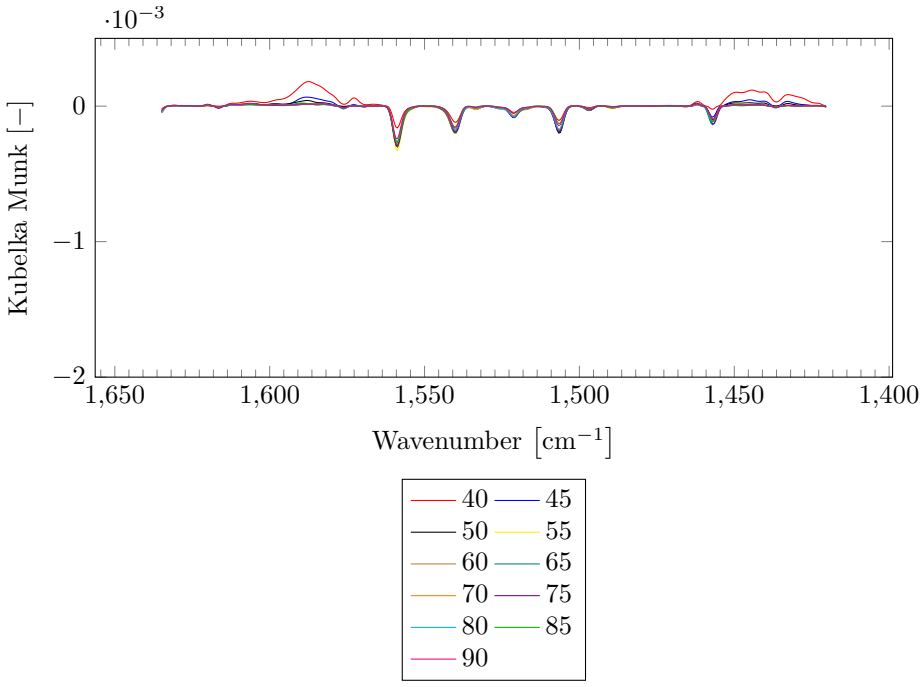

Figure 4.27: 50HPW: Desorption of pyridine, shown by plotting IR spectrums for different points of Time On Stream (TOS). The numbers given in the legend equals TOS in minutes. Pyridine was bubbled from TOS=1 to TOS=30. After this point, N_2 was flowed through the cell to keep the conditions in the cell as stable as possible. The temperature was held constant at 150 °C at all times.

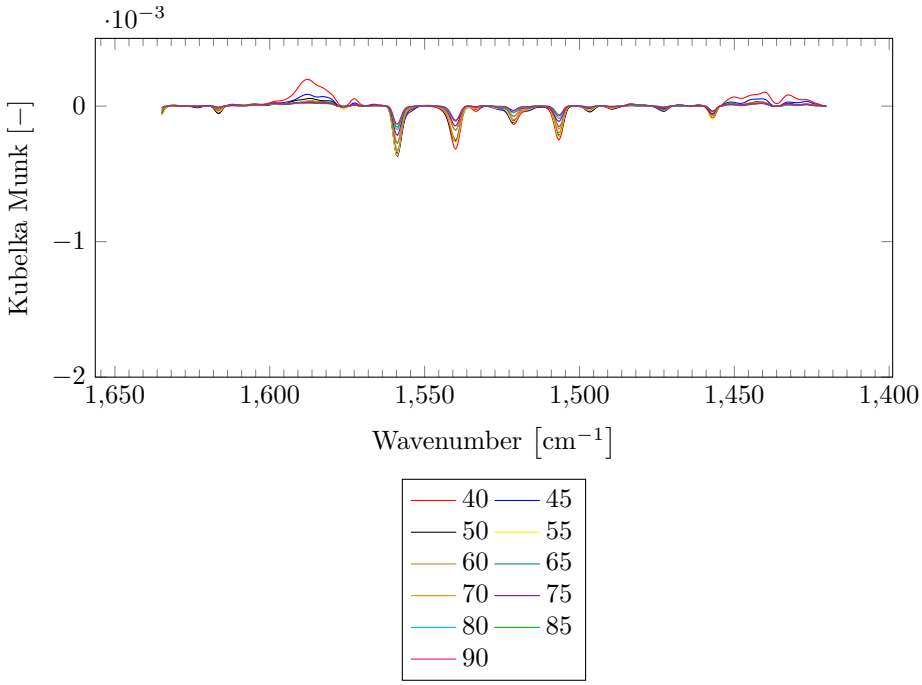

Figure 4.28: HPW: Desorption of pyridine, shown by plotting IR spectrums for different points of Time On Stream (TOS). The numbers given in the legend equals TOS in minutes. Pyridine was bubbled from TOS=1 to TOS=30. After this point, N_2 was flowed through the cell to keep the conditions in the cell as stable as possible. The temperature was held constant at 150 °C at all times.

4.1.5 S(T)EM

A Hitachi S-5500 Scanning Transmission Electron Microscope was used to investigate the surface and pore structure of the mesoporous aluminas. Obtained images of the surface of the samples, showing the pore structure of the alumina are presented in this section. EDX elemental mapping results are also shown.

Figure 4.29: SE image of surface and pore structure of m-Al_2O_3_1. A closer view of the pores are presented in Figure 4.30.

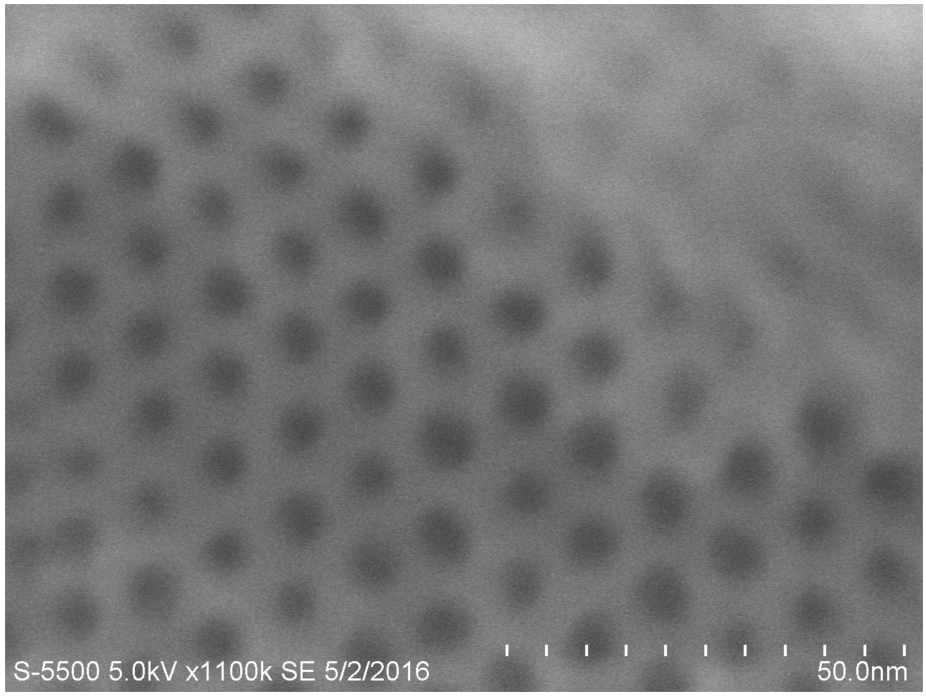

Figure 4.30: Regular pores of m-Al_2O_3_1. A magnification of the image shown in figure 4.29. The pores have a diameter of 4-6 nm.

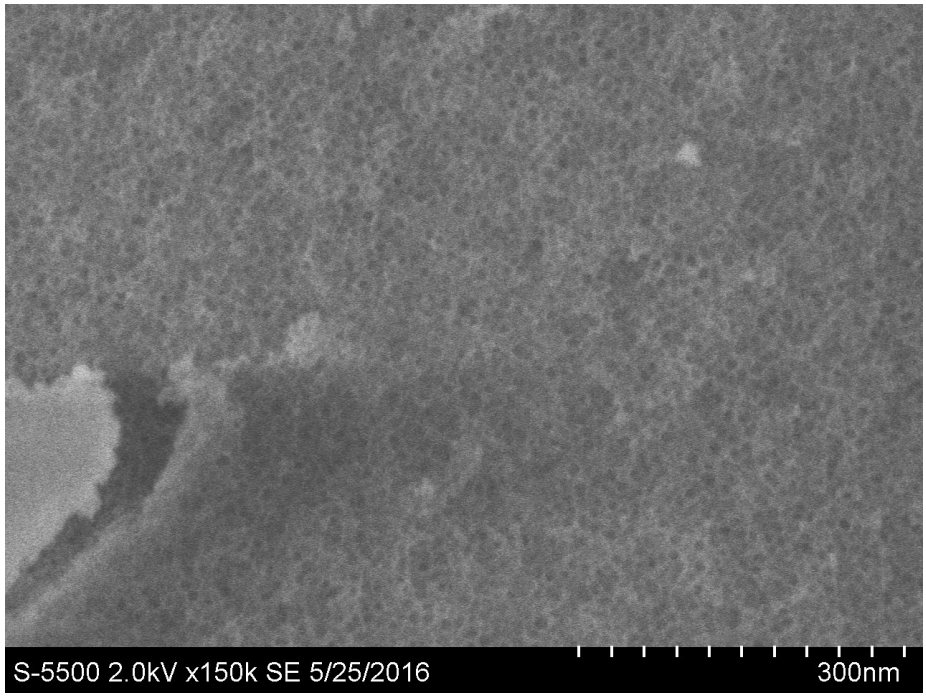

Figure 4.31: SE image showing surface and pore structure of 25HPW.

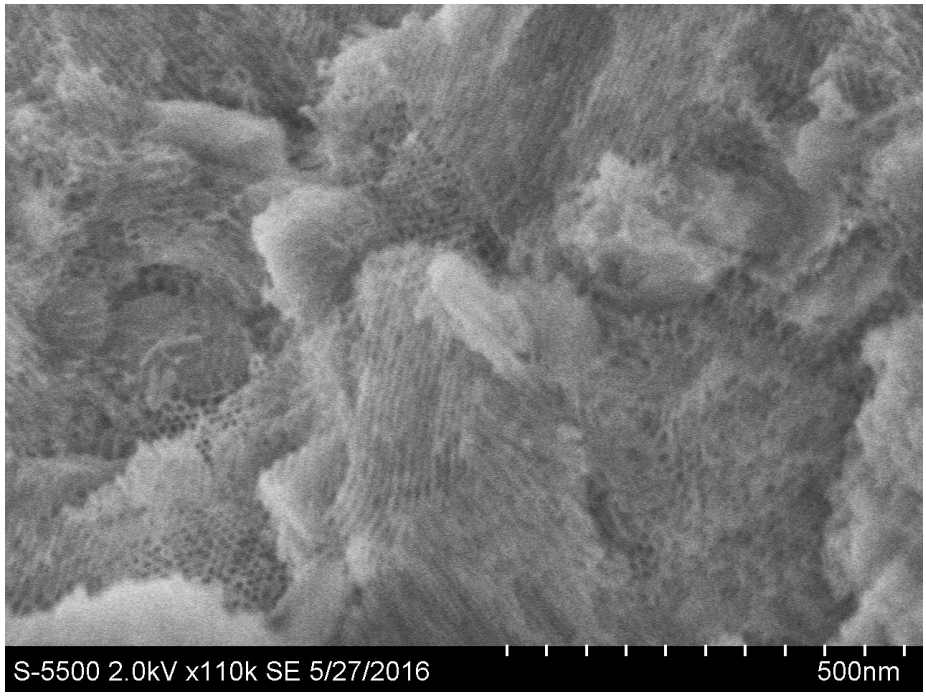

Figure 4.32: SE image showing a more topographically irregular part of the surface of 25HPW, and it's pores.

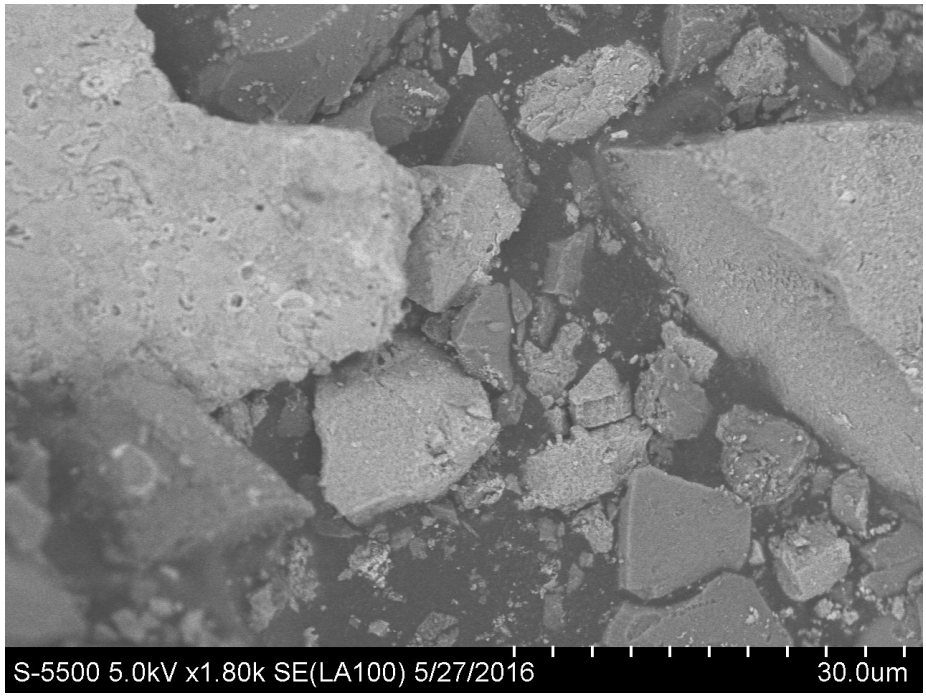

Figure 4.33: Image of 25HPW surface, BSE signal, providing more elemental contrast. Heavier elements are in general brighter. The same area was mapped by EDX to determine the composition of the particles. The map is presented in Figure 4.34.

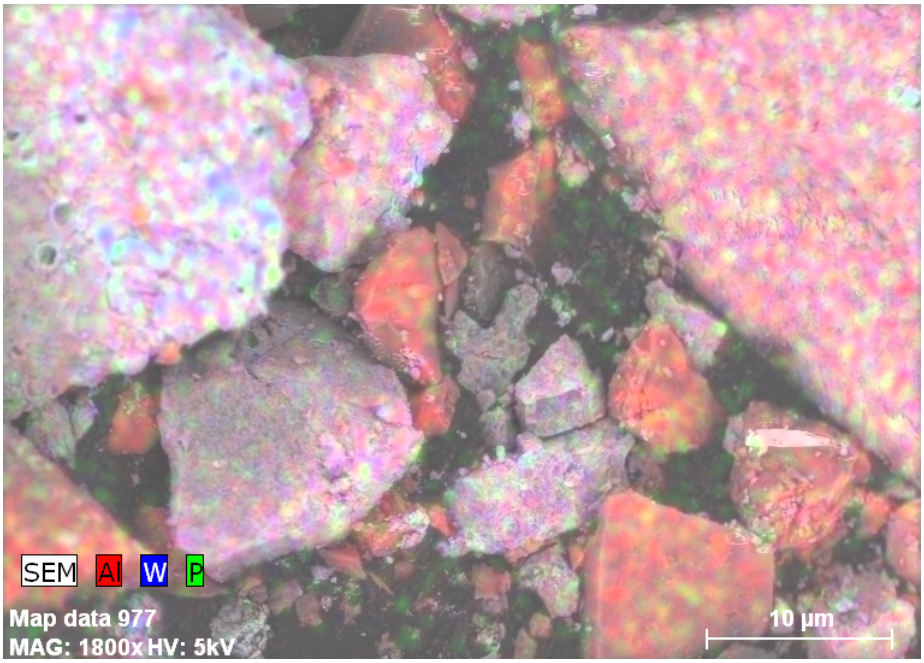

Figure 4.34: Elemental map of 25HPW1. Note that little to none signal of W (blue) is found in some of the particles, while Al (red) is registered. Phosphorous is marked with green spots.

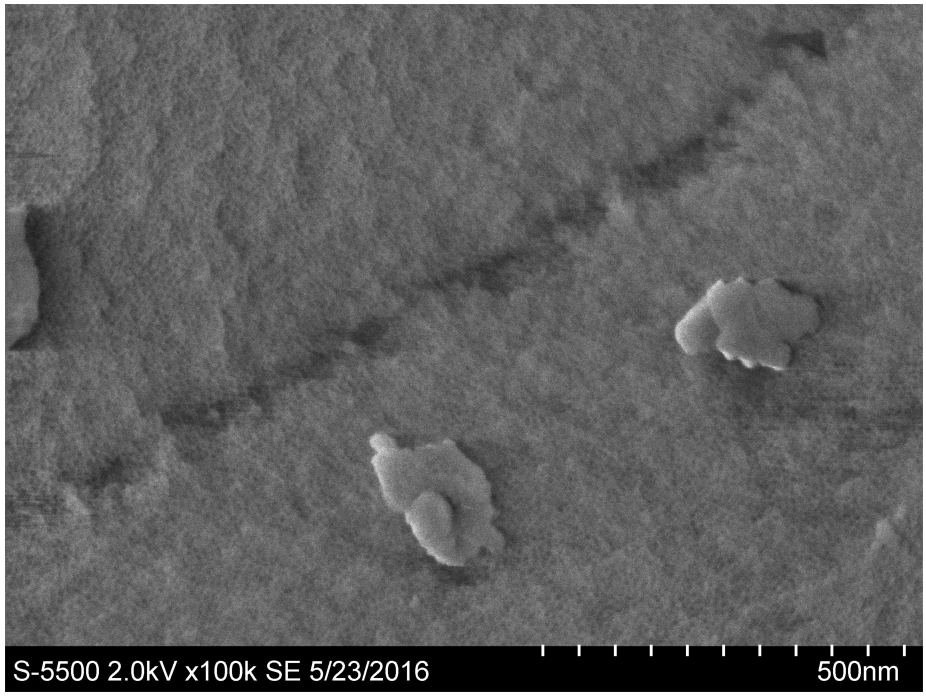

Figure 4.35: 50HPW1 surface showing pore structure of the composite surface and some larger paricles upon the surface.

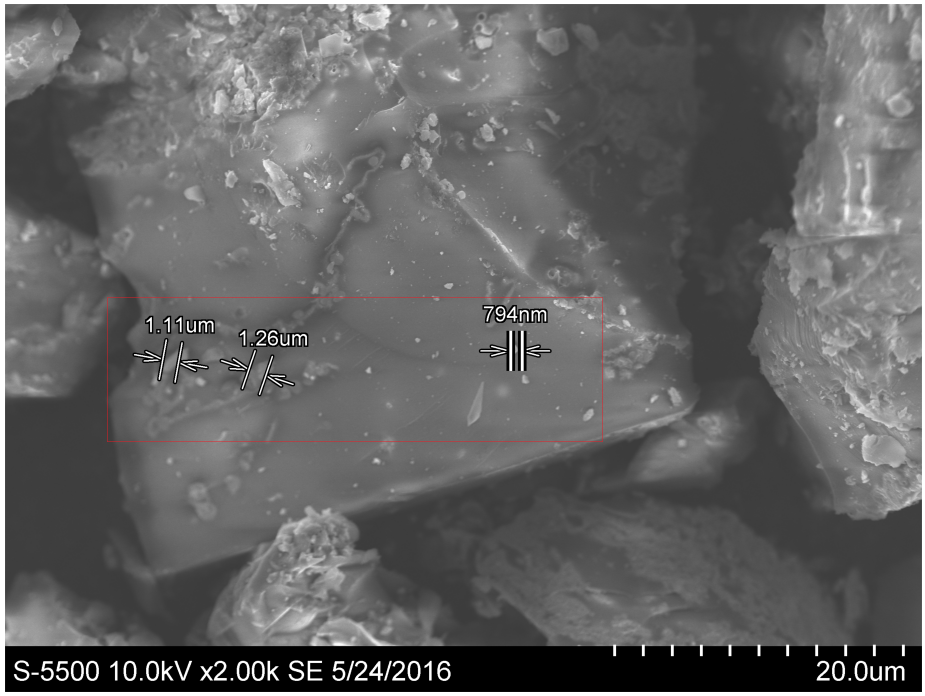

Figure 4.36: SE image of the area mapped in 4.37. The mapped area is marked by a rectangle. The rulers indicate the width of some of the Wolfram-intensive areas found by the elemental mapping.

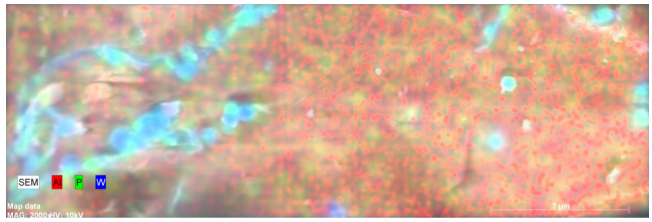

(a) Elemental mapping of 50HPW1

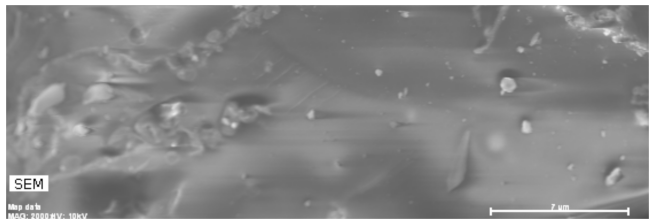

(b) SEM layer

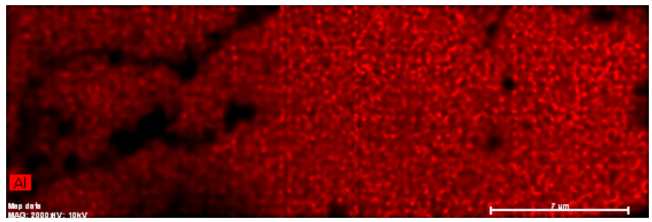

(c) Aluminum layer

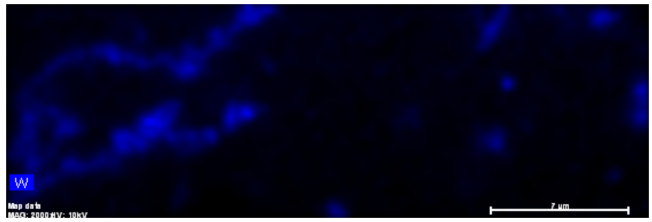

(d) Wolfram layer

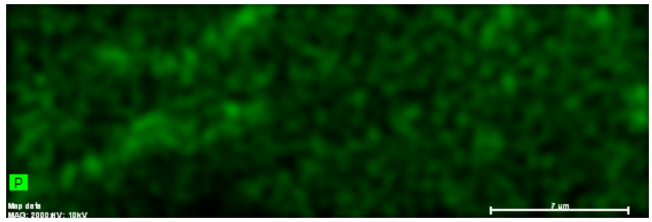

(e) Phosphorous layer

Figure 4.37: Elemental map of a particle of 50HPW1, with elemental maps for Aluminum (4.37c), Wolfram (4.37d) and Phosphorous (4.37e) as separate layers.

Chapter 5

Discussion

The results presented in chapter 4 are discussed in the following chapter. The characterisation results are first evaluated method by method. At the end of the chapter, the results are discussed with special regard to pore size and structure in Section 5.5, and acidic properties in Section 5.6.

5.1 BET/BJH analysis

Table 4.2 presents key results of measurements on the surface area and pore size of the samples. The mesoporous alumina parallels with no HPW have similar BET surface areas at around 300 $m^2\,g^{-1}$. m-Al_2O_3_2 was found to have larger pores (in both average diameter and pore volume). The BJH desorption plot (4.6) shows a wider distribution of pore sizes than for the other aluminas, with a small peak at 4 nm and a major peak at 10 nm. The minor peak at 4 nm could indicate that a pore structure similar to m-Al_2O_3_1 and m-Al_2O_3_3 (Figures 4.4 and 4.8) has been formed or partially formed, with subsequent collapse of the pore structure leading to larger pores. The pore wall collapse may have been caused by thermal effects during calcination. Apart from m-Al_2O_3_2, all samples appear to exhibit a regular pore structure with narrow pore diameter distribution. For alumina-HPW composites, the surface area seems to be decrease with increasing HPW content. The average pore diameter does not seem to follow a similar pattern.

Two parallels of 50HPW was prepared, 50HPW1 and 50HPW2. BET surface areas was measured as 127 $m^2\,g^{-1}$ and 168 $m^2\,g^{-1}$ respectively. 50HPW1 was found to have a larger avg. pore diameter as well (4.4 nm vs. 3.9 nm). Figure 4.15 compares the BET isotherms of the two samples. The isotherms are in general similar. The hysteresis of 50HPW2 is slightly narrower than 50HPW1, which may indicate that the pores of this sample may be more closed, hindering desorption. The BJH desorption plot (Figure 4.16) shows the distribution of pore sizes of the samples. Both curves are similar in shape and width, with 50HPW1 shifted slightly towards higher pore radii.

5.2 XRD

The diffractograms of the mesoporous alumina samples, presented in Figure 4.18, have few or none sharp peaks, indicating that the aluminas are amorphous. A common feature for all diffractograms (including the HPW-modified aluminas, see figures 4.19), is the high intensity at the lowest 2θ-values. This may indicate a peak at a lower angle than $2\theta = 5$, which may correspond to lattice distances similar to the pore diameter. By applying an average pore size of 4 nm in the Bragg equation, the correlating diffraction angles is $2\theta = 2.2$ for $n = 1$ (see appendix A.2 for calculation).

A small angle XRD was performed to investigate angles at θ between 1.2° and 40°. The results, plotted for lattice plane distance d, is presented in Figure 4.21. The diffractogram does not show any clear peaks, however there seems to be an increase of counts in the range of $d = [23 : 29]$Å, which corresponds to a lattice distance of 2.3 to 2.9 nm. This may indicate that a regular structure at this scale is causing Bragg diffraction. By high magnification S(T)EM images, typical pore diameters were found to be 4-6 nm, too wide to be a probable cause of this diffraction. Pore walls, however, have widths at approximately half a pore diameter (as seen in Figure 4.30), which corresponds to lattice plane distance indicated by the aforementioned d-values. However, as the surface of the aluminas have a low degree of order, with several planes in random directions (As seen in Figure 4.29 and Figure 4.32), there are several factors that may distort or hinder a clear diffraction signal, which makes the method rather uncertain. Given the small size and large width of the "peak", it should not conclusively be assigned as an indication of diffraction caused by the pore walls. Closer investigation of small angle diffraction could not be performed during the work on this thesis, but it seems to be an interesting topic for further investigation in order to obtain more information about the surface structure of the mesoporous aluminas.

HPW is easily hydrated, and its associated hydrate groups may obscure diffractograms. To obtain diffractograms of dehydroxylated 50HPW, an airtight XRD sample holder was used as described in section 3.2.1. The diffractograms from these measurements are presented in Figure 4.20. Overall, 50HPW1 seems to be amorphous as the other samples. A distinct peak is seen at $2\theta = 14°$ for the diffractogram of 50HPW1, but a similar peak is not seen in the diffractogram of HPW, indicating that the peak likely has an other origin than crystalline HPW. The EDX elemental maps of the surface of 50HPW (Figures 4.36 and 4.37) show that HPW, indicated by Wolfram, seems to form small clusters at the alumina surface. These particles seems to be non-crystalline judging by the diffractograms in Figure 4.20. However, the possibility that samples were still hydrated to some degree can not be ruled out, as the preparation procedure may have exposed them to air. In-situ dehydroxylation and XRD might produce clearer indications of the crystallinity, or lack thereof, of HPW in the alumina-HPW composites.

5.3 FT-IR

As mentioned in section 2.2.4, Pyridine interacts with acid sites on a surface in three different ways: A weak hydrogen bond may be formed between an surface OH-group and the pyridine (Py-H), a proton may be transferred from a Brønsted active site (Py-B), or the lone electron pair of Pyridine's nitrogen may be coordinated to a positive (Lewis active) Al-site (Py-L). The typical bands for the different bonds are presented in Table 2.1. Brønsted activity may be identified by a band at 1540 cm^{-1}, which is not present in vibrational modes related to Hydrogen and Lewis bonding [31, 35]. Distinguishing hydrogen and Lewis bonded pyridine can be more difficult, as these bands are very close to each other in the spectrum.

Table 5.1: Assignment of peaks and bands from spectra in Figure 4.22. Assignments were based on spectra reported by Parry (1963) [31].

Peak/Band [cm^{-1}]	**Assignment**
1445-1440	Py-H
1450	Py-L
1573	Py-L
1588-1580	Py-H
1615-1600	Py-L

No positive peaks are found at 1540 cm^{-1} in any of the spectra (Figure 4.22), indicating that there are few or none Brønsted acidic sites strong enough for proton exchange with pyridine. However, negative bands in the region related to Brønsted acidity were observed, possibly due to a contaminant.

Figures 4.25 to 4.28 show the change of the spectra during the desorption of pyridine. It is seen that the intensity in general is decreasing over time. A notable development is the negative peaks in the region 1580-1450 cm^{-1}. The spectra studied are all difference spectra, i.e. they are the result of subtracting a measurement from a reference (background) spectrum. All peaks or changes in the spectra therefore reflect a change in the system since the background spectrum was obtained prior to the introduction of pyridine.

The negative peaks are strongest for m-Al_2O_3_1 and 25HPW, while they are significantly weaker in HPW and 50HPW. The peaks appear at the same wavelengths in all spectra, indicating that their caused by a factor common for all

samples. Furthermore, as the spectra are difference spectra, negative bands indicate the presence of a compound that has later desorbed. Figure B.1 shows a typical background spectrum for the experiments. If compared to a complete spectrum, as shown in Figure B.3, it is seen that the bands of negative peaks correspond to the noisier parts of the background spectrum (2000-1300 cm^{-1} and > 3500 cm^{-1}), and where there are clear peaks (~ 2500). The IR spectrum of water vapor is shown in Figure B.2. It can be seen that water is IR-active in the same bands as the negative bands observed. This may indicate that the assumption of full dehydroxylation after 1 h at 500 °C was invalid, as water seems to desorb shortly after the introduction of pyridine.

Distinguishing Lewis coordinated pyridine and hydrogen bonded pyridine is complicated due to their overlapping bands. However, coordinated pyridine in general has bands at higher wavenumbers than hydrogen bonded pyridine, which was used as a "rule of thumb" while analyzing the spectra. Bands were assigned based on the spectrum reported by Parry (1963) [31], and compared to the assignments done in similar analyses [35, 36, 38]. Table 5.1 shows how the observed peaks in 4.22 have been assigned. The spectra plotted in Figure 4.22 indicate that both hydrogen bonded sites and Lewis sites are present. Table 5.1 shows how the observed peaks have been assigned.

Peak fitting was performed using Fityk 0.9.8, in order to deconvolve overlapping peaks. To provide an indication of the relative quantitites of the various sites, the area of the fitted peaks is compared for the various samples in Figures 4.23 and 4.24 for the regions 1460-1420 cm^{-1} and 1615-1560 cm^{-1}, respectively. In general, there is not much difference in area or the peaks thought related to Lewis bonding between the samples. The peak centers of 50HPW tends to shift slightly towards higher wavenumbers, but only to an order of a few mm^{-1}, and does not seem to indicate a significant difference of acidic strength.

5.4 S(T)EM

High magnification images of all samples (Figures 4.30 4.32 4.35) indicate that the pores are regularly distributed with a diameter between 4 to 6 nm, as indicated by BJH results.

EDX elemental mapping was used to determine the form of HPW on the surface of the composites. Figure 4.37 shows the elemental mapping of a 50HPW

particle (see Figure 4.36 for full picture). Tungsten (W) is detected in small, concentrated areas, often small particles at the size of approximately 1 µm on an otherwise smooth surface. Phosphorus, however, seems to be spread more evenly on the surface, with increasing concentration where Tungsten is found. An elemental mapping of 25HPW1 (Figure 4.34) indicate that some Tungsten is unevenly dispersed in the sample, as some it is not registered on some particles at all (Lower right corner of Figure 4.34, while Aluminum is shown to be present at the same spot. A BSE image (Figure 4.33) indicates the same effect, as the heavy Tungsten causes a brighter contrast than Aluminum. EDX mapping of powders can be problematic due to "shadow effects", i.e. edges, ridges and other topographical features blocking the signal before it reaches the detector. Some indication of shadow effects may be seen in Figure 4.34, where the signal for some of the particles underneath the larger ones seem weaker. However, shadow effects does not seem likely to hinder detection of Tungsten in the abovementioned particles, as the Aluminum and Phosphorous signal is strong.

The lack of Tungsten in some particles may stem from the synthesis. HPW was found to be partly insoluble in the sol, and may have sedimented as the gel solidified, thus being dispersed unevenly. The effect could also explain why the mass percentages of Al_2O_3 measured by XRF (Table 4.1) are higher than expected for 25HPW and 50HPW. However, XRF results must be regarded as uncertain to some degree, as the method is not capable of detecting elements lighter than Fluorine, thus being unable to take oxides, carbon or hydrates into account for the calculation of elemental composition.

5.5 Pore size and structure

One of the primary goals of the synthesis of the catalyst was to produce a regular, equal sized pore structure. The BET results and S(T)EM images states that this has been achieved. However, compared to results reported by Armatas et.al, the BET/BJH data reported in Table 4.2 show that the pores of the alumina herein presented have much narrower pores (4-6 nm against 7-10 nm) and higher surface area ($\sim$ 300 $m^2\,g^{-1}$ against 188 $m^2\,g^{-1}$), using the same procedure for synthesis.

It was suspected that residual carbon was not sufficiently removed by the calcination of the samples, as the HPW-modified alumina had black spots which

resembled charring after calcination, as well as the difference in pore size compared to Armatas. One of the samples with 50% (50HPW1) was calcined for twice as long as the other 50% HPW sample (50HPW2) to see whether this would impact the appearance, or porous properties of the samples. The pore size of 50HPW1 was found to be larger than 50HPW2, but it the difference is not large. Whether 50HPW1 has larger pores due to a longer calcination procedure can not be determined conclusively. BET and BJH analysis are based on several assumptions, and variation between analyses should be expected. The synthesis procedure was found to produce some variations between samples produced under equal conditions. This is seen in the pore distribution of m-Al_2O_3_3, which seems to indicate some degree of pore wall collapse, event though the procedure and conditions were similar to m-Al_2O_3_1 and m-Al_2O_3_2.

Through S(T)EM imaging it was seen that HPW in 50HPW tends to exists in clusters on the alumina surface. This may be the cause of the decrease in average pore volume for 50HPW1 and 50HPW2 compared to the other samples. Such clusters may block pore openings, making them inaccessible to adsorbing molecules.

5.6 Surface acidic properties

In general, the pyridine adsorption experiments seem to indicate that adding HPW has neither increased the number of acidic sites or their strength. The absorbance for all peaks are decreasing with increasing HPW-content. Armatas et. al., whose synthesis procedure was used as a basis for the synthesis of catalysts in this thesis, reported that the surface acidity of the alumina-HPW composites increased significantly with increasing HPW content. Moreover, the acidic properties of the HPW-modified catalysts were described as very good. [6]. The pyridine adsorption results reported here indicate the contrary.

$H_3PW_{12}O_{40}$ is known to have a strong Brønsted character [18], but the pyridine adsorption IR spectra (Figure 4.22) shows no clear indication of IR absorption in the regions related to Brønsted activity (shown in Table 2.1). The 1540 cm^{-1} band, which is the most characteristic band for Brønsted acidity in pyridine adsorption, shows a distinct negative band, likely due to desorbed water. It is possible that this band "conceals" a band which would otherwise indicate Brønsted acidity. The desorption plots in Figure 4.27, and Figure 4.28 show that the negative bands are significantly less intense for 50HPW and HPW,

than for 25HPW or m-Al_2O_3_1, indicating either less water contamination in the HPW-intense samples, or a positive competing contribution to these bands. As HPW is regarded to be mostly Brønsted acidic, it is not unlikely that HPW has low intensity for Lewis-acidic bond vibration. This is reflected in the general "order" of band intensities, which seems to increase with increasing alumina content.

Chapter 6

Conclusion

A mesoporous alumina with regular pore size and structure was succesfully produced by a sol-gel process and the use of a structure guiding surfactant. The mesoporous aluminas was found by BET/BJH and S(T)EM to have an average pore diameter of 4-6 nm and BET surface area of 300 $m^2\,g^{-1}$. The synthesis procedure produced several parallels of mesoporous alumina with these characteristics, but one parallell indicated that the porous structure of the gel is sensitive, and may be prone for pore collapse prior to or during calcination.

HPW was succesfully incorporated in the alumina structure. The regularity and size of the pores was not affected by the introduction of HPW, even at as high loading as 50%, by BET/BJH and S(T)EM. However, S(T)EM images revealed that HPW tends to gather in clusters on the surface at high concentrations, which seems to lead to blocking of pores and some loss of surface area and available pore volume.

The surface acidity of the catalysts was characterised by FT-IR spectroscopy, using pyridine as a probe molecule. The results obtained indicate that the alumina exhibits Lewis acidity, but do not indicate any significant Brønsted acidity for any samples. However, the spectra shows indications of water contamination, which may have distorted the bandwidths related to Brønsted acidity. Therefore, based on the obtained data, the effect of HPW as an acidic modifier in the aluminas could not be determined.

Chapter 7

Further work

A natural starting point for the continuation of this project is to test the catalysts' performance for NOx-reduction at conditions resembling the appropriate operating conditions.

Small Angle XRD could provide information on the pore structure on a grander scale than S(T)EM, if it is sufficiently regular to cause diffraction. Indications of small angle scattering were observed, which could be investigated further.

More accurate FT-IR data can likely be obtained by removing any source of contamination by water or other compounds. The dehydroxylation process of the catalysts at high temperatures should be investigated to develop a more appropriate experimental procedure to determine acidic characteristics of the HPW-alumina composites.

Bibliography

[1] I. Chorkendorff and J. W. Niemantsverdriet. *Concepts of modern catalysis and kinetics*. Wiley-VCH, Weinheim, 2nd, rev. and enl. ed. edition, 2007.

[2] V. Cappuyns and E. Slabbinck. Occurrence of vanadium in belgian and european alluvial soils. *Applied and Environmental Soil Science*, 2012, 2012.

[3] Martyn V. Twigg. Urea-scr technology for denox after treatment of diesel exhausts. *Johnson Matthey Technology Review*, 59(3):221–232, 2015.

[4] Soran Shwan. *Metal-exchanged zeolites for NH3-SCR applications - Activity and Deactivation studies*. Thesis, 2014.

[5] Georg J. B. Voss, Elvia A. Chavez Panduro, Anette Midttveit, Jostein B. Flystad, Kristin Høydalsvik, Alain Gibaud, Dag W. Breiby, and Magnus Rønning. Mesostructured alumina as powders and thin films. *J. Mater. Chem. A*, 2(25):9727–9735, 2014.

[6] Gerasimos S. Armatas, Alexandros P. Katsoulidis, Dimitris E. Petrakis, and Philippos J. Pomonis. Synthesis and acidic catalytic properties of ordered mesoporous alumina-tungstophosphoric acid composites. *Journal of Materials Chemistry*, 20(39):8631–8638, 2010.

[7] Victor Gold, Pure International Union of, and Chemistry Applied. *Compendium of chemical terminology : IUPAC recommendations*. Blackwell Scientific Publications, Oxford, 1987.

[8] C. T. Kresge, M. E. Leonowicz, W. J. Roth, J. C. Vartuli, and J. S. Beck. Ordered mesoporous molecular sieves synthesized by a liquid-crystal template mechanism. *Nature*, 359(6397):710–712, 1992.

[9] Jiři Čejka. Organized mesoporous alumina: synthesis, structure and potential in catalysis. *Applied Catalysis A: General*, 254(2):327–338, 2003.

[10] Stacy Grant, Ajayan Vinu, Stanislaw Pikus, and Mietek Jaroniec. Adsorption and structural properties of ordered mesoporous alumina synthesized in the presence of f127 block copolymer. *Colloids and Surfaces A: Physicochemical and Engineering Aspects*, 385(1-3):121–125, 2011.

[11] G.D. Stucky, B.F. Chmelka, D. Zhao, N. Melosh, Q. Huo, J. Feng, P. Yang, D. Pine, D. Margolese, and W. Lukens. Block copolymer processing for mesostructured inorganic oxide materials, 2007.

[12] Ying Wan and Dongyuan Zhao. *Ordered Mesoporous Materials*, pages 277–300. Wiley-VCH Verlag GmbH & Co. KGaA, 2009.

[13] C. Jeffrey Brinker, Yunfeng Lu, Alan Sellinger, and Hongyou Fan. Evaporation Induced Self-Assembly: Nanostructures Made Easy. *Advanced Materials*, 11(7):579–585, 1999.

[14] Quan Yuan, An-Xiang Yin, Chen Luo, Ling-Dong Sun, Ya-Wen Zhang, Wen-Tao Duan, Hai-Chao Liu, and Chun-Hua Yan. Facile synthesis for ordered mesoporous gamma-aluminas with high thermal stability. *Journal of the American Chemical Society*, 130(11):3465–3472, 2008.

[15] Peter Atkins, Tina Overton, Jonathan Rourke, Mark Weller, and Fraser Armstrong. *Shriver and Atkins Inorganic Chemistry*. Oxford, 2006.

[16] Steven Heylen, Sylvia Smeekens, Christine Kirschhock, Johan A. Martens, and Tatjana Parac-Vogt. Temperature swing adsorption of nox over keggin type heteropolyacids. *Energy and Environmental Science*, 3(7):910–916, 2010.

[17] S. Hodjati, C. Petit, V. Pitchon, and A. Kiennemann. Removal of nox from a lean exhaust gas by absorption on heteropolyacids: Reversible sorption of nitrogen oxides in h3pw 12o406h2o. *Journal of Catalysis*, 197(2):324–334, 2001.

[18] W. Turek, J. Haber, and A. Krowiak. Dehydration of isopropyl alcohol used as an indicator of the type and strength of catalyst acid centres. *Applied Surface Science*, 252(3):823–827, 2005.

[19] John Regalbuto. *Catalyst Preparation : Science and Engineering*. Catalyst Preparation: Science and Engineering. Taylor and Francis, Hoboken, 2006.

[20] Miron V. Landau. *Sol-Gel Processing*, pages 83–109. Wiley-VCH Verlag GmbH & Co. KGaA, 2009.

[21] Paul C. Hiemenz and Raj Rajagopalan. *Principles of Colloid and Surface Chemistry*. Marcel Dekker, Weinheim, 3rd edition, revised and expanded edition, 1997.

[22] Anette Midttveit. Ordered Mesoporous Alumina as a Support in Nickel promoted Cobalt Fischer Tropsch Catalysts. Master thesis, NTNU, 2012.

[23] Burkhard Beckhoff, Birgit Kanngieber, Norbert Langhoff, Reiner Wedell, and Helmut H. Wolff. *Handbook of Practical X-Ray Fluorescence Analysis*. Springer-Verlag Berlin and Heidelberg GmbH & Co. KG, Dordrecht, 2007.

[24] Stephen Brunauer, Edward Emmett, and Edward Teller. Adsorption of gases in multimolecular layers. *Journal of the American Chemical Society*, 60(2):309–319, 1938.

[25] Elliott P. Barrett, Leslie G. Joyner, and Paul P. Halenda. The determination of pore volume and area distributions in porous substances. i. computations from nitrogen isotherms. *Journal of the American Chemical Society*, 73(1):373–380, 1951.

[26] Barbara H. Stuart. *Infrared Spectroscopy : Fundamentals and Applications*. Analytical Techniques in the Sciences. Wiley, Chichester, 2004.

[27] Guido Busca. The use of vibrational spectroscopies in studies of heterogeneous catalysis by metal oxides: an introduction. *Catalysis Today*, 27(3):323–352, 1996.

[28] Mitsuo Tasumi. *Introduction to Experimental Infrared Spectroscopy : Fundamentals and Practical Methods*. Wiley, Somerset, NJ, USA, 2014.

[29] J. W. Niemantsverdriet. *Spectroscopy in catalysis : an introduction*. Wiley-VCH, Weinheim, 3rd, completely rev. and enl. ed. edition, 2007.

[30] Frédéric Thibault-Starzyk and Françoise Maugé. *Infrared Spectroscopy*, pages 1–48. Wiley-VCH Verlag GmbH & Co. KGaA, 2012.

[31] E. P. Parry. An infrared study of pyridine adsorbed on acidic solids. characterization of surface acidity. *Journal of Catalysis*, 2(5):371–379, 1963.

[32] Joseph I. Goldstein. *Scanning electron microscopy and X-ray microanalysis*. Kluwer Academic/Plenum Publishers, New York, 3rd ed. edition, 2003.

[33] Patrick Echlin. *Handbook of Sample Preparation for Scanning Electron Microscopy and X-Ray Microanalysis*. Springer, Dordrecht, 2009.

[34] David A. Coucheron. In-situ ftir studies of surface modified fischer-tropsch catalysts. Spec. project (master), NTNU, 2014.

[35] Claudio Morterra and Giuliana Magnacca. A case study: surface chemistry and surface structure of catalytic aluminas, as studied by vibrational spectroscopy of adsorbed species. *Catalysis Today*, 27(3–4):497–532, 1996.

[36] Xinsheng Liu and Ralph E. Truitt. Drft-ir studies of the surface of gamma-alumina. *Journal of the American Chemical Society*, 119(41):9856, 1997.

[37] Guido Busca. The surface of transitional aluminas: A critical review. *Catalysis Today*, 226:2–13, 2014.

[38] Abbas A. Khaleel and Kenneth J. Klabunde. Characterization of aerogel prepared high-surface-area alumina: in situ ftir study of dehydroxylation and pyridine adsorption. *Chemistry (Weinheim an der Bergstrasse, Germany)*, 8(17):3991, 2002.

[39] Nist chemistry webbook: Infrared spectrum of water. `http://webbook.nist.gov/cgi/cbook.cgi?ID=C7732185&Units=SI&Type=IR-SPEC&Index=1#IR-SPEC`. Accessed: 08.06.2016.

Appendix A

Calculations

This chapter presents calculations done in relation to experimental work in the thesis.

A.1 Preparation of Al-HPW composite

The mass of HPW precursor for synthesis was calculated according to the desired HPW-loading, x_{HPW} [%] and derived as follows.

$$
\begin{aligned}
x_{HPW} &= \frac{m_{HPW}}{m_{\mathrm{Al_2O_3}} + m_{HPW}} \\
m_{HPW} &= x_{HPW}\left(m_{\mathrm{Al_2O_3}} + m_{HPW}\right) \\
m_{HPW} &= \frac{x_{HPW} m_{\mathrm{Al_2O_3}}}{1 - x_{HPW}}
\end{aligned}
$$

The precursor, $\mathrm{H_3PW_{12}O_{40}}$, was purchased in hydrated form, with a non-specified number of hydrates. Based on measurements performed by Armatas [6], calculations were based on 26 hydrates, giving the following molecular formula $\mathrm{H_3PW_{12}O_{40}x26\,H_2O}$ with a molar mass $M_{HPW26H20} = 3348.05\ \mathrm{g\,mol^{-1}}$. To obtain the desired amount of non-hydrated HPW, the difference in molar mass must be taken into account.

$$n_{HPW} = \frac{m_{HPW26H20}}{M_{HPW26H20}} = \frac{m_{HPW}}{M_{HPW}}$$
$$m_{HPW26H20} = m_{HPW}\frac{M_{HPW26H20}}{M_{HPW}}$$

Sample calculation for $a_{HPW} = 25wt\%$:

$$m_{HPW} = \frac{0.25 \cdot 0.51}{1 - 0.25} = 0.17 \text{ g}$$
$$m_{HPW26H20} = 0.17 \text{ g} \cdot \frac{3348.05 \text{ g mol}^{-1}}{2880.05 \text{ g mol}^{-1}} = 0.20 \text{ g}$$

A.2 Bragg diffraction angle calculation

Bragg's law (2.4) is given as

$$n\lambda = 2d \sin\theta \ ; \ n = 1, 2, ...$$

Rearranging and multiplying both sides with 2 to find 2θ gives

$$2\theta = 2sin^{-1}\frac{n\lambda}{2d}$$

Inputting parameters (choosing n=1 for this example): $\lambda = 0.154$ nm, $d = 4$nm, $n = 1$

$$2\theta = 2sin^{-1}\left(\frac{0.154 \text{ nm}}{2 \times 4 \text{ nm}}\right)$$
$$2\theta = 2.2$$

Appendix B

FT-IR

B.1 IR reference spectra

Background spectra obtained prior to pyridine adsorption experiments are plotted in figure B.1. A reference IR spectrum for water, obtained from NIST Chemistry Webbook [39] is given in Figure B.2. A full pyridine adsorption spectrum for all samples may be found in Figure B.3.

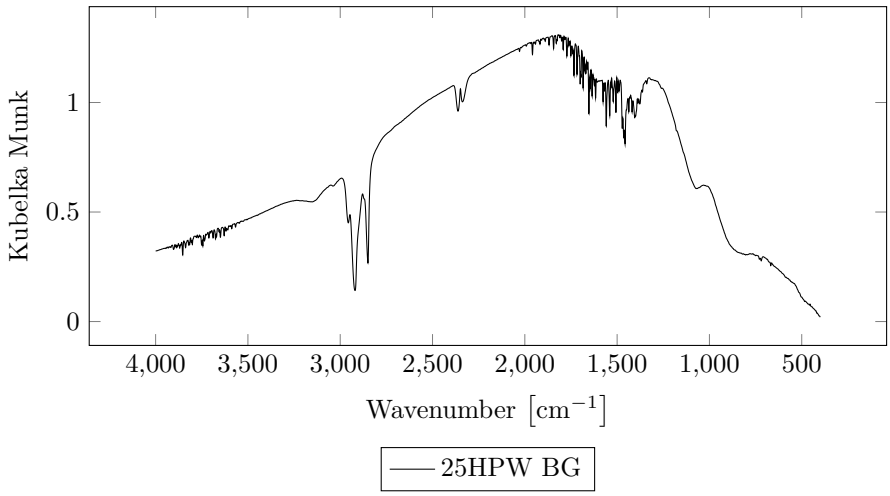

Figure B.1: Example of Background Spectrum obtained prior to pyridine adsorption analysis. To resemble the analysis conditions as close as possible, the spectrum is taken of the diluted sample (1% 25HPW in KBr in this case) after dehydroxylation and cooling to analysis temperature (150 °C) under an N_2-atmosphere (15 mL min^{-1}.

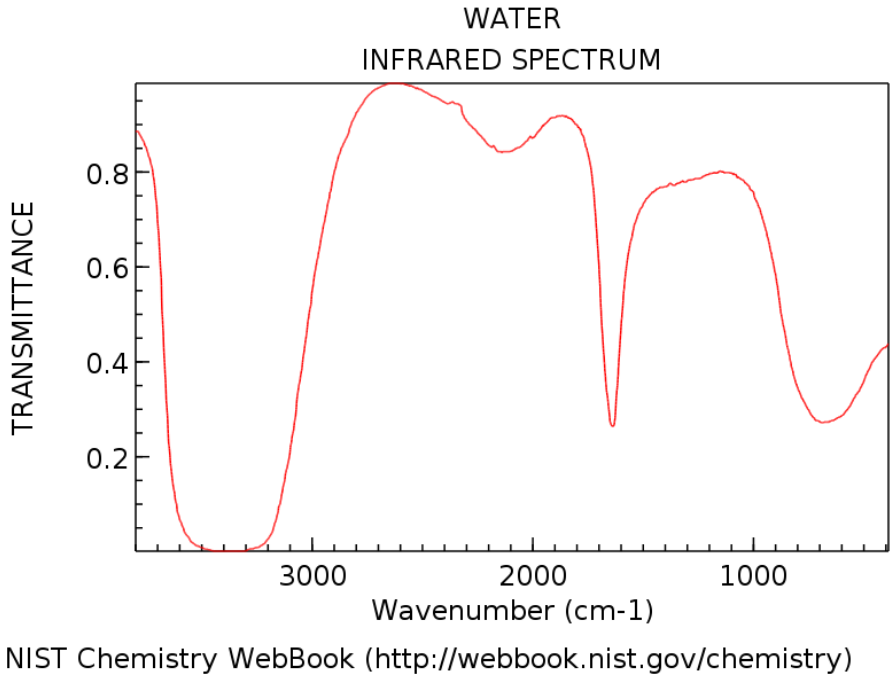

Figure B.2: IR transmittance spectrum of water. Obtained from NIST Chemistry Webbook [39]

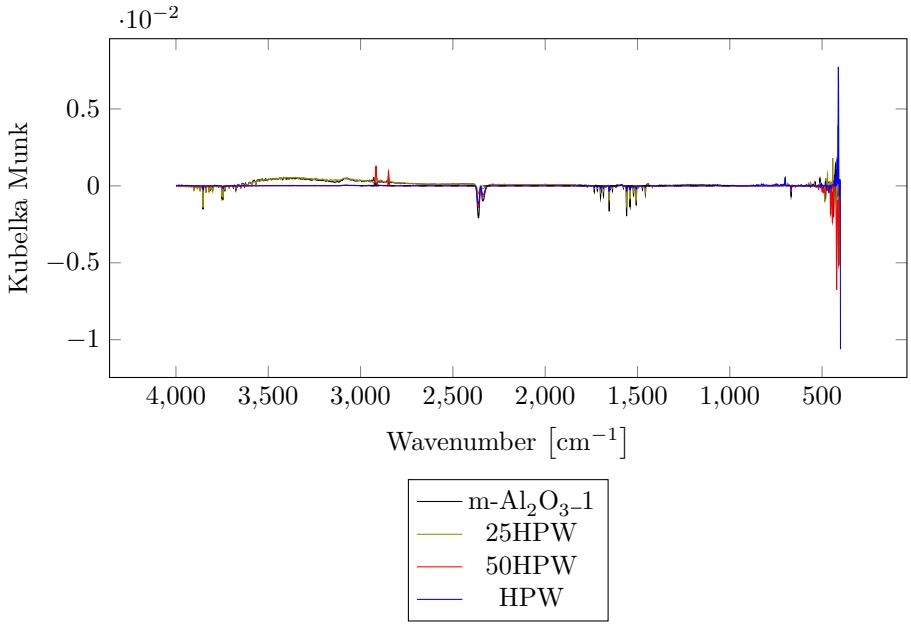

Figure B.3: IR spectra of all samples 30 minutes after exposure to pyridine was ended.

Appendix C

Risk Assessment

ID	1590	**Status**	**Dato**
Risikoområde	Risikovurdering: Helse, miljø og sikkerhet (HMS)	Opprettet	06.10.2015
Opprettet av	Ole Håvik Bjørkedal	Vurdering startet	06.10.2015
Ansvarlig	Ole Håvik Bjørkedal	Tiltak besluttet	
		Avsluttet	10.06.2016

Project/Master - Catalysis, 2015, Ole Håvik Bjørkedal

Gyldig i perioden:

-

Sted:

3 - Gløshaugen / 315 - Kjemi 5

Mål / hensikt

This risk assessment contains all the activities that the master student Ole Håvik Bjørkedal will perform in the labs of the Catalysis group.

Bakgrunn

The project aims to find new catalysts for low temperature selective catalytic reduction (SCR) of NOx. Pt/Al2O3 seems to be a good candidate, and the catalyst has to be prepared for characterization and analysis.

Beskrivelse og avgrensninger

The catalyst will be prepared by impregnating Alumina (Al2O3) with platinum nitrate, and drying off the solvent.

Forutsetninger, antakelser og forenklinger

[Ingen registreringer]

Vedlegg

[Ingen registreringer]

Referanser

[Ingen registreringer]

Oppsummering, resultat og endelig vurdering

I oppsummeringen presenteres en oversikt over farer og uønskede hendelser, samt resultat for det enkelte konsekvensområdet.

Farekilde: **Use of furnaces**

Uønsket hendelse: **Burn from hot furnace**

Konsekvensområde:		
Helse	Risiko før tiltak:	Risiko etter tiltak:
Ytre miljø	Risiko før tiltak:	Risiko etter tiltak:
Materielle verdier	Risiko før tiltak:	Risiko etter tiltak:

Farekilde: **Preparation of precursor solution and impregnation of alumina support**

Uønsket hendelse: **Chemical burn**

Konsekvensområde:		
Helse	Risiko før tiltak:	Risiko etter tiltak:
Ytre miljø	Risiko før tiltak:	Risiko etter tiltak:
Materielle verdier	Risiko før tiltak:	Risiko etter tiltak:

Uønsket hendelse: **Formation of harmful chemicals/gas**

Konsekvensområde:		
Helse	Risiko før tiltak:	Risiko etter tiltak:
Ytre miljø	Risiko før tiltak:	Risiko etter tiltak:
Materielle verdier	Risiko før tiltak:	Risiko etter tiltak:

Farekilde: **Preparation of Meosoporous Alumina and Alumina-Tungstophosphoric acid composites**

Uønsket hendelse: **Fire or explosion**

Konsekvensområde:		
Helse	Risiko før tiltak:	Risiko etter tiltak:
Materielle verdier	Risiko før tiltak:	Risiko etter tiltak:

Uønsket hendelse: **Chemical burn**

Konsekvensområde:		
Helse	Risiko før tiltak:	Risiko etter tiltak:

Uønsket hendelse: **Metal Corrosion**

Konsekvensområde:		
Materielle verdier	Risiko før tiltak:	Risiko etter tiltak:

Farekilde:	**Preparation of Meosoporous Alumina and Alumina-Tungstophosphoric acid composites**
Uønsket hendelse:	**Formation of volatile or otherwise harmful vapors**
Konsekvensområde:	Helse
Risiko før tiltak:	
Risiko etter tiltak:	

Farekilde:	**IR-analysis w. Pyridine adsorption**
Uønsket hendelse:	**Exposure to pyridine**
Konsekvensområde:	Helse
Risiko før tiltak:	
Risiko etter tiltak:	

Uønsket hendelse:	**Fire**
Konsekvensområde:	Helse
Risiko før tiltak:	
Risiko etter tiltak:	
Materielle verdier	
Risiko før tiltak:	
Risiko etter tiltak:	

Endelig vurdering

Risikoen forbundet med de ovenfor listede aktivitetene regnes som lav.

Risikovurderingen er gjort på generelt grunnlag og basert hovedsaklig på vurdering av undertegnede.

Oversikt involverte enheter og personell

En risikovurdering kan gjelde for en, eller flere enheter i organisasjonen. Denne oversikten presenterer involverte enheter og personell for gjeldende risikovurdering.

Enhet /-er risikovurderingen omfatter

- Institutt for kjemisk prosessteknologi

Deltakere

Magnus Rønning
Cristian Ledesma Rodriguez
Karin Wiggen Dragsten

Lesere

[Ingen registreringer]

Andre involverte/interessenter

[Ingen registreringer]

Følgende akseptkriterier er besluttet for risikoområdet Risikovurdering: Helse, miljø og sikkerhet (HMS):

Helse	Materielle verdier	Omdømme	Ytre miljø
			

Oversikt over eksisterende, relevante tiltak som er hensyntatt i risikovurderingen

I tabellen under presenteres eksisterende tiltak som er hensyntatt ved vurdering av sannsynlighet og konsekvens for aktuelle uønskede hendelser.

Farekilde	Uønsket hendelse	Tiltak hensyntatt ved vurdering
Use of furnaces	Burn from hot furnace	Heat-restistant gloves
Preparation of precursor solution and impregnation of alumina support	Chemical burn	Safety Goggles
	Chemical burn	Lab Coat
	Chemical burn	Fume hoods
	Chemical burn	Nitrile gloves
	Formation of harmful chemicals/gas	Safety Goggles
	Formation of harmful chemicals/gas	Lab Coat
	Formation of harmful chemicals/gas	Fume hoods
	Formation of harmful chemicals/gas	Nitrile gloves
Preparation of Meosoporous Alumina and Alumina-Tungstophosphoric acid composites	Fire or explosion	Safety Goggles
	Fire or explosion	Lab Coat
	Fire or explosion	Fume hoods
	Chemical burn	Safety Goggles
	Chemical burn	Lab Coat
	Chemical burn	Nitrile gloves
	Chemical burn	Emergency Eye shower and flask
	Metal Corrosion	
	Formation of volatile or otherwise harmful vapors	Fume hoods
	Formation of volatile or otherwise harmful vapors	Fire Extinguisher
	Formation of volatile or otherwise harmful vapors	Fume Hood
IR-analysis w. Pyridine adsorption	Exposure to pyridine	Safety Goggles

IR-analysis w. Pyridine adsorption	Exposure to pyridine	Lab Coat
	Exposure to pyridine	Fume hoods
	Exposure to pyridine	Nitrile gloves
	Fire	Safety Goggles
	Fire	Lab Coat
	Fire	Fume hoods
	Fire	Emergency Eye shower and flask
	Fire	Emergency shower
	Fire	Fire Extinguisher

Eksisterende og relevante tiltak med beskrivelse:

Safety Goggles
Eye protection to be worn at all times while working in lab.

Lab Coat
Protection of skin against spills, corrosice chemicals, etc.

Fume hoods
Platinum nitrate can form harmful gases. Handle in fume hood

Nitrile gloves
Platinum nitrate is corrosive and oxidizing. Hand protection important

Emergency Eye shower and flask
In case chemicals come in contact with eyes. Rinse with plenty of water, consult medical personnell

Emergency shower
In case of serious spills, or clothing on fire. Located in lab.

Fire Extinguisher
[Ingen registreringer]

Heat-restistant gloves
Using furnaces to calcine the support and impregnated catalyst. Protection against burns

Risikoanalyse med vurdering av sannsynlighet og konsekvens

I denne delen av rapporten presenteres detaljer dokumentasjon av de farer, uønskede hendelser og årsaker som er vurdert. Innledningsvis oppsummeres farer med tilhørende uønskede hendelser som er tatt med i vurderingen.

Følgende farer og uønskede hendelser er vurdert i denne risikovurderingen:

- **Use of furnaces**
  - Burn from hot furnace
- **Preparation of precursor solution and impregnation of alumina support**
  - Chemical burn
  - Formation of harmful chemicals/gas
- **Preparation of Meosoporous Alumina and Alumina-Tungstophosphoric acid composites**
  - Fire or explosion
  - Chemical burn
  - Metal Corrosion
  - Formation of volatile or otherwise harmful vapors
- **IR-analysis w. Pyridine adsorption**
  - Exposure to pyridine
  - Fire

Oversikt over besluttede risikoreduserende tiltak med beskrivelse:

Use of furnaces (farekilde)

Alumina will be calcined in HT-furnaces
Catalyst/impregnated alumina will be dryed/calcined in furnaces

Use of furnaces/Burn from hot furnace (uønsket hendelse)

Accidentally touching a hot surface on the furnace may cause burns.

Samlet sannsynlighet vurdert for hendelsen: Lite sannsynlig (2)

Kommentar til vurdering av sannsynlighet:

The furnaces are placed in a closed cabinet, which reduces the likelihood of accidentally touching a hot furnace. It has a visible display which displays the temperature in the furnace, and protective gloves are available.

Vurdering av risiko for følgende konsekvensområde: Helse

Vurdert sannsynlighet (felles for hendelsen): Lite sannsynlig (2)

Vurdert konsekvens: Liten (1)

Kommentar til vurdering av konsekvens:

A burn from touching the furnace for a very short time (reflex to draw hand away from heat) is not likely to require more medical attention than basic first aid (cooling with water for ca. 20 min.)

Preparation of precursor solution and impregnation of alumina support (farekilde)

Diluting Platinum nitrate solution, and impregnating alumina

Preparation of precursor solution and impregnation of alumina support/Chemical burn (uønsket hendelse)

Platinum nitrate is corrosive and oxidising.

Samlet sannsynlighet vurdert for hendelsen: Lite sannsynlig (2)

Kommentar til vurdering av sannsynlighet:

Working with small quantities and using pipettes in a fume hood ensures that the chemical is handled in a controlled environment. Personal protective gear (labcoat, goggles, gloves) prohibit eventual spills to come in contact with skin.

Vurdering av risiko for følgende konsekvensområde: Helse

Vurdert sannsynlighet (felles for hendelsen): Lite sannsynlig (2)

Vurdert konsekvens: Middels (2)

Kommentar til vurdering av konsekvens:

Small quantities of the chemical will be handled and open for exposure, usually handled with pipettes. Contact with skin is not likely to cause serious damage, especially if proper first aid is performed (rinsing with water).

Preparation of precursor solution and impregnation of alumina support/Formation of harmful chemicals/gas (uønsket hendelse)

Platinum nitrate may react and form harmful gas.

Samlet sannsynlighet vurdert for hendelsen: Lite sannsynlig (2)

Kommentar til vurdering av sannsynlighet:

Working with dilute solution, and in small quantities.

Vurdering av risiko for følgende konsekvensområde: Helse

Vurdert sannsynlighet (felles for hendelsen): Lite sannsynlig (2)

Vurdert konsekvens: Middels (2)

Kommentar til vurdering av konsekvens:

Fume hoods ensures that any harmful gas is ventilated away from the lab. Working with small quantities of chemicals.

Preparation of Meosoporous Alumina and Alumina-Tungstophosphoric acid composites (farekilde)

Meosoporous Alumina and Alumina-Tungstophosphoric acid composites (Al-TPA) will be prepared by sol-gel copolymerization using a surfactant.

Chemicals involved in synthesis:
Pluronic F127 surfactant
HNO3(aq) (65-70%)
Anhydrous Ethanol
Al(OPr)3 (Pr=Propyl)
Tungstophosphoric acid H3PW12O40-xH2O (TPA/HPW)

Preparation of Meosoporous Alumina and Alumina-Tungstophosphoric acid composites/Fire or explosion (uønsket hendelse)

HNO3 is a strong oxidant, may cause combustion in contact with flammable materials.
Ethanol is highly flammable, and may be explosive in high concentrations.
AL(OPr)3 is highly flammable.

Årsak: Ignition of vapor due to ignition sources in the lab

Beskrivelse:

Sparks, heat or other sources of ignition in the lab may ignite flammable vapors

Samlet sannsynlighet vurdert for hendelsen: Svært lite sannsynlig (1)

Kommentar til vurdering av sannsynlighet:

Potential ignition sources are isolated in the lab, little exposure to ignition sources. Using fume hoods remove flammable vapors.

Vurdering av risiko for følgende konsekvensområde: Helse

Vurdert sannsynlighet (felles for hendelsen): Svært lite sannsynlig (1)

Vurdert konsekvens: Middels (2)

Kommentar til vurdering av konsekvens:

Working with small amounts of flammable chemicals, fires likely not to be too big if they occur.
Lab Coat and Safety Goggles minimizes exposed skin.

Preparation of Meosoporous Alumina and Alumina-Tungstophosphoric acid composites/Chemical burn (uønsket hendelse)

HNO3 is highly corrosive, may cause chemical burns if hands or eyes are exposed
Tungstophosphoric acid (HPW) is corrosive

Årsak: Spills

Beskrivelse:

Spilling corrosive chemicals on skin or eyes may cause chemical burns.

Samlet sannsynlighet vurdert for hendelsen: Lite sannsynlig (2)

Kommentar til vurdering av sannsynlighet:

Acids are handled in small quantites with pipettes. Gloves, lab coat and safety goggles are always used.

Vurdering av risiko for følgende konsekvensområde: Helse

Vurdert sannsynlighet (felles for hendelsen): Lite sannsynlig (2)

Vurdert konsekvens: Liten (1)

Kommentar til vurdering av konsekvens:

The most likely consequence is minor burns on hands e.g. under the sleeve of the lab coat. Such exposure may be treated by rinsing the exposed area with large amounts of water, and is not likely to cause much injury.

The worst case scenario is spilling acid in eyes. This is considered unlikely, especially as safety goggles are worn at all times in the lab.

Preparation of Meosoporous Alumina and Alumina-Tungstophosphoric acid composites/Metal Corrosion (uønsket hendelse)

HNO3 is highly corrosive and may cause corrosion damage to metals.

Årsak: Corrosion/Degradation of metallic equipment

Beskrivelse:

Concentrated HNO3 may corrode metallic equipment

Samlet sannsynlighet vurdert for hendelsen: Svært lite sannsynlig (1)

Kommentar til vurdering av sannsynlighet:

Metallic equipment will not be exposed to concentrated HNO3 over time.

Vurdering av risiko for følgende konsekvensområde: Materielle verdier

Vurdert sannsynlighet (felles for hendelsen): Svært lite sannsynlig (1)

Vurdert konsekvens: Liten (1)

Kommentar til vurdering av konsekvens:

No expensive or essential metallic equipment will be used.

Preparation of Meosoporous Alumina and Alumina-Tungstophosphoric acid composites/Formation of volatile or otherwise harmful vapors (uønsket hendelse)

During aging or drying, volatile compounds may form and/or evaporate. These may be flammable or harmful if inhaled.

Samlet sannsynlighet vurdert for hendelsen: Lite sannsynlig (2)

Kommentar til vurdering av sannsynlighet:

The amount of chemicals are small. If kept under a fume hood, harmful or volatile chemicals are very unlikely to reach dangerous concentrations.

Vurdering av risiko for følgende konsekvensområde: Helse

Vurdert sannsynlighet (felles for hendelsen): Lite sannsynlig (2)

Vurdert konsekvens: Liten (1)

Kommentar til vurdering av konsekvens:

Breathing in vapors may cause headaches or nausea.

IR-analysis w. Pyridine adsorption (farekilde)

Using FTIR-DRIFTS to analyse surface acidity of catalysts and support materials. Pyridine is used as a probe molecule

IR-analysis w. Pyridine adsorption/Exposure to pyridine (uønsket hendelse)

Pyridine (C5H5N) is an aromatic compound. MSDS lists dangers related to inhalation, skin exposure and swallowing.

Samlet sannsynlighet vurdert for hendelsen: Lite sannsynlig (2)

Kommentar til vurdering av sannsynlighet:

[Ingen registreringer]

Vurdering av risiko for følgende konsekvensområde: Helse

Vurdert sannsynlighet (felles for hendelsen): Lite sannsynlig (2)

Vurdert konsekvens: Liten (1)

Kommentar til vurdering av konsekvens:

Small leaks in gas lines may release small amounts of pyridine vapor into the air. The apparatus sits in a ventilated chamber in the Chemistry hall. Smell/inhalation may lead to irritated airways, headaches and nausea. Leak tests should be performed regularly, especially near the bubbler.

A small amount (~20 mL) of pyridine is used for the analysis, and it is kept in a closed glass bubbler. The pyridine does not have to be changed often, and is therefore contained for most of the time. Risks are related to filling and emptying the bubbler, which should be done in a well ventilated fume hood. Extraction of pyridine from the chemical bottle is done with a syringe to minimize exposure.

IR-analysis w. Pyridine adsorption/Fire (uønsket hendelse)

Pyridine is a highly flammable and volatile compund with a low flash point.

Samlet sannsynlighet vurdert for hendelsen: Lite sannsynlig (2)

Kommentar til vurdering av sannsynlighet:

The pyridine is kept in a close container, and is not in contact with any hot surfaces or other sources of ignition. Room temperature in the chamber can occasionally be high (around 30 degrees), above the flashpoint of pyridine.

Vurdering av risiko for følgende konsekvensområde: Helse

Vurdert sannsynlighet (felles for hendelsen): Lite sannsynlig (2)

Vurdert konsekvens: Middels (2)

Kommentar til vurdering av konsekvens:

[Ingen registreringer]

Oversikt over besluttede risikoreduserende tiltak:

Under presenteres en oversikt over risikoreduserende tiltak som skal bidra til å reduseres sannsynlighet og/eller konsekvens for uønskede hendelser.

Oversikt over besluttede risikoreduserende tiltak med beskrivelse: